Università di Pisa

Facoltà di Scienze Matematiche Fisiche e Naturali

Corso di Laurea Specialistica in Scienze Fisiche

Anno Accademico 2005/2006

Tesi di Laurea Specialistica

Detection of low energy neutrinos and Dark Matter search in ANTARES

Candidato:

Niccolò Cottini

Relatore:

Chiar.mo Prof.

Vincenzo Flaminio

Contents

Introduction

In recent years, there has been a growing interaction between particle physics and cosmology. The interest lies in the potential for particle physics discoveries to solve some of the problems of cosmology, and the possibility for cosmological observations to constrain ideas in particle physics.

A major example is represented by the possible solution given to the Dark Matter (DM) problem by Supersymmetry (SUSY) theory: the frontier of particle physics knowledge will probably be extended beyond the Standard Model in the near future, hopefully explaining the nature of the dark and dominant matter content of the Universe through the discovery of SUSY particles. However, DM searches may first detect the new hypothetical particles and help to define their properties.
Thus, our focus is on a so-called indirect search method, that is the detection of a neutrino signal arising from DM annihilation in the core of celestial bodies. This is one of the reasons for which big neutrino telescopes have been and are being built in different sites all over the world.

Our experimental work is developed in the context of the ANTARES experiment, which plans to use a deep sea neutrino telescope - currently under construction - to detect neutrinos from a 10 GeV threshold, up to the PeV region. The experimental technique relies on the detection of Cherenkov light from neutrino interaction products. One of the main sources of background is represented by deep sea luminescence, generated by both isotope decays and living organisms. This kind of background has been deeply studied with prototype detectors; the data obtained are analyzed also in a section of our work, for a precise modelization of the environment conditions, improving

our following MonteCarlo simulations.

The main contribution given to the physics of the experiment is represented by the study of a new reconstruction technique, recently proposed for low energy (10 GeV-10 TeV) tracks. In this range, signals from SUSY DM annihilation are expected. The feasibility of this reconstruction strategy is demonstrated and the improvements with respect to the standard one are shown.

The last part of this work is devoted to the analysis of the data taken with the first sector of the ANTARES detector, operating since March 2006.

The outline of the thesis, organized in seven chapters, is as follows.

Chapter 1. A brief description of the standard cosmological model, with its observational milestones and its open problems, in particular the nature of Dark Matter.

Chapter 2. A phenomenological introduction to SUSY theory and to its main ideas. A Dark Matter candidate particle arises in this framework.

Chapter 3. Short review of the ANTARES experiment, with a description of the detector and of its performances.

Chapter 4. Analysis of the data taken with the MILOM prototype detector, for a detailed study of the optical background properties at the experiment site.

Chapter 5. Description of the trigger system for the ANTARES data acquisition.

Chapter 6. Study of a new reconstruction technique for low energy tracks. Efficiency and purity are characterized with MonteCarlo simulations.

Chapter 7. Analysis of data taken with the first operating sector of the ANTARES detector.

Chapter 1

The Standard Model of Cosmology

One of the most impressive achievements of Cosmology is a quite detailed understanding of the physical properties of the Universe at its earliest stages. Thanks to theoretical analysis and astronomical observations, we have today a Standard Model of Cosmology. Its milestone is the Big Bang model, supported by the key observations of:

- the expansion of the Universe;
- the existence of the Cosmic Microwave Background radiation (CMB);
- the relative abundance of light elements in the Universe.

Behind this success there is Einstein's theory of General Relativity. Nevertheless some "old" problems are still open: there are evidences of a Universe mainly consisting of non-baryonic, non-luminous and non-absorbing matter, commonly referred to as Dark Matter (DM), immersed in some form of energy featuring a negative pressure, named Dark Energy. Ordinary matter is thought to be responsible for just a subdominant fraction of the total energy density of the Universe.
In the next sections, we will analyse in more details this general frame.

1.1 The cosmological parameters Ω_M and Ω_Λ

Considering the small scale structure of the Universe, matter distribution is rather irregular: stars are grouped in galaxies, which form clusters and then super-clusters. Only on larger scales ($\gtrsim 10^8$ light-years) we can observe a homogeneous distribution. The *cosmological principle* assumes that homogeneity and isotropy are properties of the Universe and states: a family of spatial sections of space-time exists such that every section has the same physical properties in every point and direction.
According to the principle and to Einstein's equations, considering the Universe content as a perfect fluid, its space-time description is given by the *Robertson-Walker* metric

$$ds^2 = dt^2 - a^2(t)\Big(\frac{dr^2}{1-kr^2} + r^2 d\theta^2 + r^2 \sin^2\theta\, d\phi^2\Big)$$

and by the Friedmann equations:

$$\Big(\frac{\dot{a}}{a}\Big)^2 + \frac{k}{a^2} = \frac{8\pi G}{3}\Big(\rho_m + \rho_{rad} + \frac{\Lambda}{8\pi G}\Big), \tag{1.1}$$

$$\frac{2\ddot{a}}{a} + \Big(\frac{\dot{a}}{a}\Big)^2 + \frac{k}{a^2} = -8\pi G\Big(p - \frac{\Lambda}{8\pi G}\Big). \tag{1.2}$$

ρ_m represents the non relativistic matter density, while ρ_{rad} stands for radiation plus relativistic matter. p is the pressure of the fluid, Λ the cosmological constant, which can be associated to the vacuum energy of quantum field theory.
Matter is supposed to be macroscopically at rest with respect to the coordinate system t, r, θ, ϕ (comoving coordinates). The Universe expansion is governed by the scale factor $a(t)$; k determines the spatial curvature:

$$\begin{aligned} k = -1 &\rightarrow \text{open Universe} \\ k = 0 &\rightarrow \text{flat Universe} \\ k = 1 &\rightarrow \text{closed Universe.} \end{aligned}$$

In a uniformly expanding Universe, Hubble's law is valid:

$$v = Hd, \tag{1.3}$$

with the Hubble parameter

$$H(t) = \frac{\dot{a}(t)}{a(t)}. \tag{1.4}$$

However, taking the difference between eq.(1.1) and (1.2), the equation

$$\frac{\ddot{a}}{a} = -\frac{4\pi G}{3}(\tilde{\rho} + 3\tilde{p}) \tag{1.5}$$

$$\Big(\tilde{\rho} = \rho_m + \rho_{rad} + \frac{\Lambda}{8\pi G},\ \tilde{p} = p - \frac{\Lambda}{8\pi G}\Big)$$

shows that if matter alone drives the expansion, it is presently decelerating (since $\tilde{\rho} > 0$ and $\tilde{p}$ would be ~ 0); if Λ dominates, then the expansion may accelerate.
We can expand the scale factor $a(t)$ in a Taylor series around the present time t_0:

$$a(t) = a(t_0)\Big(1 + H_0(t - t_0) - \frac{1}{2}q_0 H_0^2(t - t_0)^2 + \dots\Big). \tag{1.6}$$

The Hubble parameter $H_0 \equiv H(t_0)$ at the present cosmic time t_0 is called the *Hubble constant*. Recent observations give

$$H_0 = h \cdot 100\text{km s}^{-1}\ \text{Mpc}^{-1}, \tag{1.7}$$

where $h = 0.71^{+0.04}_{-0.03}$. $q_0 \equiv -\ddot{a}(t_0)/(a(t_0)\, H_0^2)$ is the so-called deceleration parameter.

We define the critical density ρ_{crit}[1] of the Universe by

$$\rho_{crit} \equiv \frac{3H^2}{8\pi G} \tag{1.8}$$

[1]The present value is $\rho^0_{crit} = 1.87837(28) \cdot h^2\, g\, cm^{-3} \sim 4$ protons/m^3

and we use it to write eq.(1.1) as

$$\frac{k}{H^2a^2} = \Omega - 1, \quad \Omega \equiv \frac{\tilde{\rho}}{\rho_{crit}}. \tag{1.9}$$

Therefore the geometry of the Universe is determined by Ω, which clearly depends on time. We can also distinguish the contributions to Ω given by matter, radiation and the cosmological constant, defining respectively:

$$\Omega_M \equiv \frac{8\pi G\rho_m}{3H^2}, \qquad \Omega_R \equiv \frac{8\pi G\rho_r}{3H^2}, \qquad \Omega_\Lambda \equiv \frac{\Lambda}{3H^2}.$$

As it will be shown in the following, Ω_R is negligible in the present Universe; so - given $\Omega_k = -k/(a^2H^2)$ - we can rewrite eq.(1.9) at $a_0 \equiv a(t_0)$ as

$$\Omega_M + \Omega_\Lambda + \Omega_k = 1 \tag{1.10}$$

and

$$q_0 = \frac{1}{2}\Omega_M - \Omega_\Lambda. \tag{1.11}$$

Thus, we have tied both the geometry and the rate of expansion of the Universe to its matter and vacuum energy content. It is also possible to draw some evolution scenarios and make predictions about the fate of the Universe.
To discriminate between the possible solutions presented in fig.(1.1), it is necessary to measure some way the values of the parameters Ω_M and Ω_Λ. Good observables for this purpose are

- Supernovae of type 1a;
- CMB anisotropies.

1.2 Measurements of the cosmological parameters

1.2.1 Standard candles

One of the consequences of the expansion of the Universe is the cosmological redshift: the further from us light was emitted, the more we observe its

wavelength shifted to the red region.
A redshift parameter z is defined by

$$1 + z = \frac{\lambda_{obs}}{\lambda_{emit}} \equiv \frac{a(t_{obs})}{a(t_{emit})}. \tag{1.12}$$

Using z and eq.(1.6), it is possible to write the distance of a body emitting light as

$$d = \frac{1}{H_0}\Big(z + \frac{1}{2}(1 - q_0)^2 z^2 + \dots\Big). \tag{1.13}$$

Then, recalling that $q_0 = \frac{1}{2}\Omega_M - \Omega_\Lambda$, the cosmological parameters can be extracted from distance and redshift measurements.

In general, it is difficult to estimate accurately cosmological distances; fortunately it is possible to use the so-called *Standard Candles*, especially the Supernovae of type 1a. These sources are identified by their particular light curve and their spectral lines from heavy elements.
Supernovae of this type are believed to occur due to the merging of two white dwarfs, with masses very close to the Chandrasekhar limit. Since the masses involved in the explosion are always roughly the same, it is reasonable to assume that any Supernova 1a has an intrinsic luminosity. Thus, it is possible to give the distance from the apparent luminosity.

The High-z Supernova Search Team [1] has observed some Supernovae in the range $z = 0.3 \div 1.2$. The possible values for Ω_M and Ω_Λ have been determined and are shown in fig.(1.1).
The emerging picture shows an accelerating Universe, in which Λ plays a major role.

1.2.2 CMB anisotropies

In the Big Bang model, the Cosmic Microwave Background was generated at recombination time ($\sim 10^5$ years after Big Bang), when Hydrogen atoms formed from primeval plasma and photons from the early Universe underwent the last scattering. Since that time, they have been redshifted and are observed today in the microwave regime.

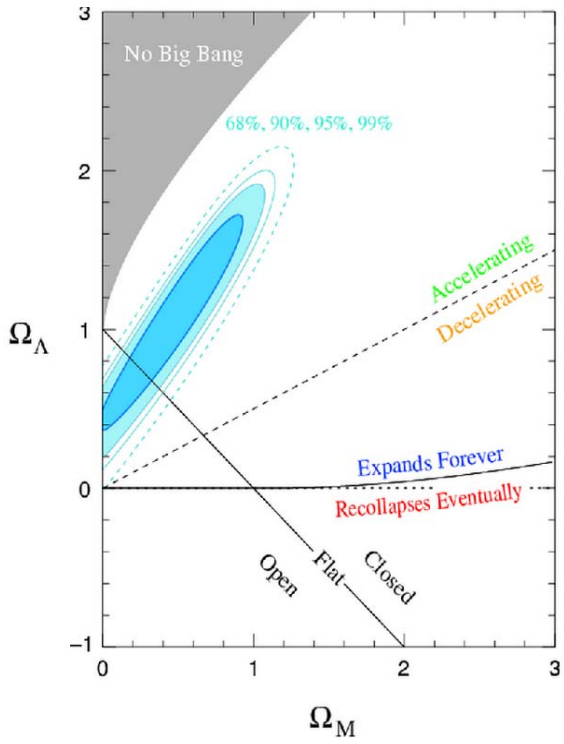

Figure 1.1: The evidenced oval zone is the most probable region for the parameters Ω_M and Ω_Λ, according to Supernova observations.

CMB temperature anisotropies have been observed at level of a few parts in 100000. They are closely related to density fluctuations at the time in which Universe became transparent to radiation.
Therefore mapping the CMB temperature means investigating the matter distribution and then the space-time properties of the Universe at recombination.

The COBE and WMAP satellites and the balloon experiment BOOMERanG measured the anisotropies and described them in terms of spherical harmonics. They obtained an angular power spectrum, from which it is possible to determine the cosmological parameters [2]. The results are shown in fig.(1.2)

and constrain the geometry of the Universe to a flat scenario:

$$\Omega_{tot} = 1.02 \pm 0.02.$$

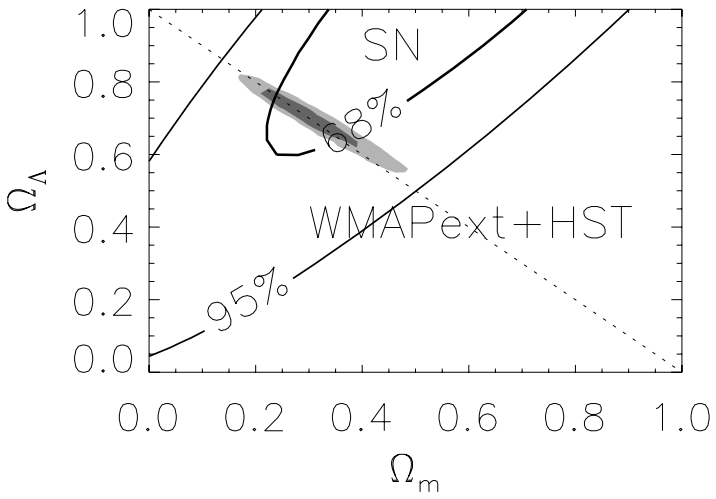

Figure 1.2: Constrain on the geometry of the Universe from the experiments on CMB anisotropies. Also the results from Supernova 1a observations are shown.

The other best cosmological parameters from WMAP observations are in the following table [3].

Matter density Ω_M	0.27 ± 0.04
Baryon density Ω_b	0.044 ± 0.004
Dark Energy density Ω_Λ	0.73 ± 0.04
Radiation density Ω_R	$\Omega_R \ll \Omega_M$

In conclusion, there are two different experimental results (from Standard Candles and anisotropies of CMB measurement) that are compatible: they identify two regions in the plane of possible Ω_M and Ω_Λ values [fig.(1.2)], which have a common intersection.

In this common area, we have $\Omega_M \sim 0.3$, thus supporting the results from measurements of the Hydrogen velocities in galaxies, presented in the next section.

1.3 The Dark Matter

Observations of the orbital velocities v_{orb} of gas clouds in spiral galaxies, as a function of their radial distance r from the galaxy core, have revealed a flat distribution as the distance increases [fig.(1.3)].

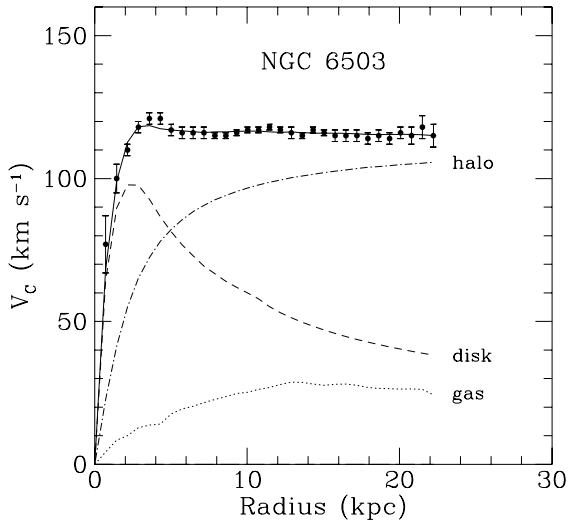

Figure 1.3: Rotation curve of the spiral galaxy NGC 6503. The dashed line shows the contribution expected from the disk material alone, the dot-dashed line is from the dark matter halo alone [4].

This result contradicts the Kepler's third law for the motion of a body around a massive core, according to which v_{orb} should decrease proportionally to $r^{-1/2}$.
Unless classical Newtonian mechanics breaks down at the scale of size of

spiral galaxies, the distribution of mass determining the gas dynamics must extend far beyond the visible galaxy core; the proportionality to be respected is

$$M(r)\ \alpha\ r,$$

where $M(r)$ is the total mass within the sphere of radius r.
Thus, v_{orb} distributions can be explained if galaxy cores are surrounded by a *halo*, containing a new massive source of gravity that does not emit any radiation: the Dark Matter (DM).

Observations of gas clouds give a ratio between the mass of dark (M_{dm}) and visible (M_{lm}) matter as follows:

- $3 < \frac{M_{dm}}{M_{lm}} < 5$ for spiral galaxies;
- $10 < \frac{M_{dm}}{M_{lm}}$ for elliptic galaxies;
- $\frac{M_{dm}}{M_{lm}} \sim 50 \div 100$ for clusters of galaxies.

The mass density of luminous matter in galaxies is found to be only $\Omega_{LM} \sim 0.01$, while for the Dark Matter we obtain $\Omega_{DM} \sim 0.1$ inside galaxies and $\Omega_{DM} \sim 0.3$ between them.
These results let people claim that Dark Matter holds together the bricks of the Universe, but despite its importance, its nature is still unknown.
There is only a relative certainty about what DM can not be.

1.3.1 Dark Matter candidates

One of the main supports to the Big Bang model is given by the *nucleosynthesis*: a process involving nucleons and leptons few minutes after the Big Bang, which is able to predict the abundance of elements in the Universe.
The nucleosynthesis accounts for the measured ^{4}He mass fraction of about 24 per cent, that can not be explained only by stellar production. The remaining part of nuclei is made by Hydrogen, except for very small fractions of ^{3}He, ^{2}H and ^{7}Li. Heavier elements, on the contrary, are produced in the interior of stars (or in other astrophysical processes such as Supernova explosions) and have negligible abundances.

Measurements of the Deuterium to Hydrogen ratio, together with predictions from nucleosynthesis [5], give:

$$\Omega_B h^2 = 0.019 \pm 0.001.$$

A consistent independent value is found through CMB analysis (see WMAP results above). Although baryons in star account for only about 1/4 of all the estimated baryons (the rest are optically dark), Ω_B only weights for about 1/10 of Ω_{DM}: the Dark Matter is found to be mainly non-baryonic.

Another possible DM candidate is the neutrino. Unfortunately, even considering the huge number of neutrinos produced in the Big Bang, they could explain all the non-baryonic DM content of the Universe only if they had a mass in the range $10 - 50$ eV. This hypothesis is ruled out by many neutrinos experiments, which set an upper limit to the mass at 0.05 eV.

Furthermore observations show that the formation of structures in the Universe is still going on, from smaller to bigger entities. Then if Dark Matter had been *hot* (i.e. moving relativistically) like neutrinos, these fast moving particles would have smoothed every density irregularities of the early Universe; the first objects to form would have been the largest structures (super clusters) and small objects (galaxies) would have formed later by fragmentation.
For this reason Dark Matter particles must be *cold* (i.e. moving at non relativistic speed) and weakly interacting. Being their nature yet unknown, they are referred to as WIMPs: Weakly Interacting Massive Particles.

Before analysing - in the next chapter - a theoretical model which provides a WIMP candidate, we summarize in fig.(1.4) our current knowledge of the Universe composition.

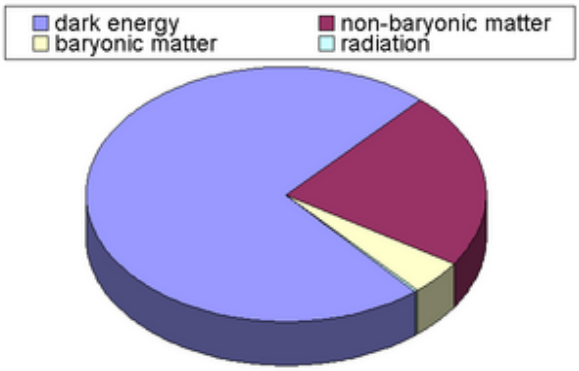

Figure 1.4: Contribution to the (total) energy density of the Universe from various sources: $\sim 73\%$ is due to dark energy, $\sim 27\%$ to matter of all types; the contribution of baryons is $\sim 4.4\%$, that of radiation only $\sim 0.005\%$.

Chapter 2

Supersymmetry and Dark Matter

Supersymmetry or fermion-boson symmetry (SUSY) has not been observed in Nature yet. It is a purely theoretical invention. Its validity in particle physics follows from the common belief in unification.
Over 30 years, thousands of papers have been written on supersymmetry. For reviews, see e.g. [8]- [12].

2.1 The hierarchy problem of the Standard Model

The Standard Model (SM) of fundamental interactions describes strong, weak and electromagnetic interactions of elementary particles. It is based on a gauge principle, according to which all the forces of Nature are mediated by an exchange of the gauge fields of the corresponding local symmetry group. The symmetry group of the SM is

$$SU_{color}(3) \otimes SU_{left}(2) \otimes U_{hypercharge}(1).$$

The electroweak sector of the SM contains a parameter with the dimen-

sions of energy, namely the vacuum expectation value of the Higgs field

$$v \approx 246 \text{ GeV}. \tag{2.1}$$

This parameter sets the scale, in principle, of all masses in the theory. For instance, the mass of the W (neglecting radiative corrections) is given by

$$M_W = \frac{gv}{2} \sim 80 \text{ GeV}, \tag{2.2}$$

and the mass of the Higgs boson is

$$M_H = v\sqrt{\frac{\lambda}{2}}, \tag{2.3}$$

where g is the $SU(2)$ gauge coupling constant, and λ is the strength of the Higgs self-interaction in the Higgs potential

$$V = -\mu^2\phi^\dagger\phi + \frac{\lambda}{4}(\phi^\dagger\phi)^2 \tag{2.4}$$

($\lambda > 0$ and $\mu^2 > 0$).
The negative sign in front of the mass term is essential for the spontaneous symmetry breaking mechanism to work. With the sign as in eq.(2.4), the minimum of V interpreted as a classical potential is at the non-zero value

$$|\phi| = \sqrt{2}\mu/\sqrt{\lambda} \equiv v/\sqrt{2}, \tag{2.5}$$

where $\mu \equiv \sqrt{\mu^2}$.
If $-\mu^2$ in eq.(2.4) is replaced by the positive quantity μ^2, the classical equilibrium value is at the origin in field space, which would imply $v = 0$ and all particles massless.

The discussion so far has been at tree level. What happens when we include loops? The SM is renormalizable, but although it is calculable up to infinite energies, nobody seriously believes that the SM is really all there is, however high we go in energy. That is to say, in loop integrals of the form

$$\int^{\Lambda} d^4k \; f(k, \, external \, momenta), \tag{2.6}$$

we do not think that the cut-off Λ should go to infinity physically.
More reasonably, we regard the SM as a part of a larger theory, which includes as yet unknown new physics at high energy, Λ representing the scale at which this new physics appears. At the very least, for instance, there surely must be some kind of new physics at the scale when quantum gravity becomes important, which is

$$M_P = (G_N)^{-1/2} \simeq 1.2 \times 10^{19} \text{ GeV}. \tag{2.7}$$

If this is the scale of the new physics beyond the SM or if there is any scale of new physics even several orders of magnitude different from v, then we meet a problem with the SM, once we go beyond tree level: the 4-boson self-interaction in eq.(2.4) generates, at one-loop order, a contribution to the $\phi^\dagger\phi$ term, which is proportional to

$$\lambda \int^{\Lambda} d^4k \, \frac{1}{k^2 - M_H^2}. \tag{2.8}$$

This integral clearly diverges quadratically and it turns out to be positive, producing a correction

$$\sim \lambda\Lambda^2\phi^\dagger\phi \tag{2.9}$$

to the $-\mu^2\phi^\dagger\phi$ term in V. Now we know that the vev v is given in terms of μ by eq.(2.5), and that its value is fixed phenomenologically by eq.(2.1). Hence it seems that μ can hardly be much greater than of order a few hundred GeV (or, if it is, λ is much greater than unity - which would imply that we can not do perturbation theory).
On the other hand, if $\Lambda \sim M_P \sim 10^{19}$ GeV, the one-loop quantum correction to $-\mu^2$ is then vastly greater than $\sim (100 \text{ GeV})^2$ and positive; therefore obtaining a value $\sim -(100 \text{ GeV})^2$ after inclusion of loop corrections would seem to require that we start with an equally huge but negative value of the Lagrangian parameter $-\mu^2$, relying on a remarkable cancellation to get us from $\sim -(10^{19} \text{ GeV})^2$ to $\sim -(10^2 \text{ GeV})^2$.

This is an unpleasant *fine-tuning* problem, originating from the hierarchy $M_{H,W} \ll M_P$.

2.2 Unification of gauge couplings

Since the main motivation for SUSY is related to unification theory, we briefly recall the main ideas of Grand Unification (GUT).
The philosophy of GUT is based on a hypothesis: gauge symmetry increases with energy. Having in mind unification of all forces of Nature on a common basis and neglecting gravity for the time, being due to its weakness, the idea of GUT is the following: all known interactions are different branches of a unique interaction, associated with a simple gauge group. The unification (or splitting) occurs at high energy.

Low energy			$\Rightarrow$	High energy
$SU_C(3)$	$SU_L(2)$	$U_Y(1)$	$\Rightarrow$	G_{GUT}
gluons	W, Z	photon	$\Rightarrow$	gauge bosons
quarks	leptons		$\Rightarrow$	fermions
g_3	g_2	g_1	$\Rightarrow$	g_{GUT}

At first sight this is impossible, due to a big difference in the values of the couplings of strong, weak and electromagnetic interactions. However, the crucial point here is the running coupling constants: it is a generic property of quantum field theory, which has an analogy in classical physics.
Indeed, consider electric and magnetic phenomena. Let us take some dielectric medium and put a sample electric charge in it. What happens is that the medium is polarized; it contains electric dipoles which are arranged in such a way as to screen the charge [fig.(2.1)].

The opposite situation occurs in a magnetic medium: according to the Biot-Savart law, electric currents of the same direction are attracted to each other, while those of the opposite one are repulsed [fig.(2.1)]. This leads to antiscreening of electric currents in a magnetic medium.
In QFT, the role of the medium is played by the vacuum. Vacuum is polarized due to the presence of virtual pairs of particles in it. The matter fields and transverse quanta of vector fields in this case behave like dipoles in a dielectric medium and cause screening, while the longitudinal quanta of

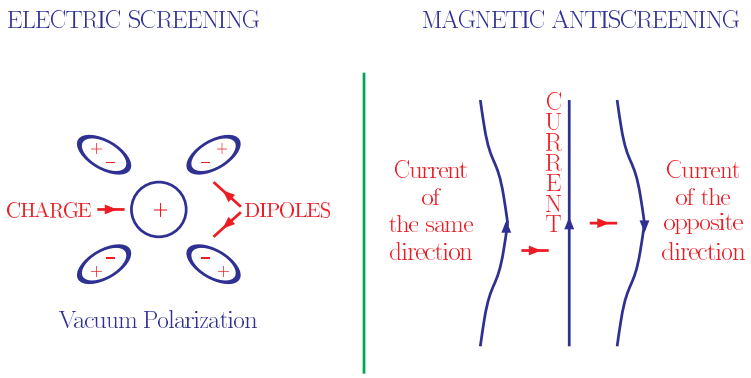

Figure 2.1: Electric screening and magnetic antiscreening.

vector fields behave like currents and cause antiscreening. These two effects compete each other; thus, the couplings become functions of a distance or an energy scale:

$$\alpha_i = \alpha_i(\frac{Q^2}{\Lambda^2}) = \alpha_i(distance), \quad \alpha_i \equiv g_i^2/4\pi. \tag{2.10}$$

This dependence is described by the renormalization group equations and is confirmed experimentally [fig.(2.2)].

In the SM the strong and weak couplings - associated with non-Abelian gauge groups - decrease with energy, while the electromagnetic one - associated with the Abelian group - increases. Thus, it becomes possible that at some energy scale they become equal. According to the GUT idea, this equality is not occasional, but is a manifestation of a unique origin of these three interactions. As a result of spontaneous symmetry breaking, the unifying group is broken and the unique interaction is splitted into three branches, which we call strong, weak and electromagnetic interactions.

After the precise measurement of the $SU_C(3) \otimes SU_L(2) \otimes U_Y(1)$ coupling constants, it has become possible to check the unification numerically. The three quantities to be compared are

$$\alpha_1 \quad = \quad (5/3)g'^2/(4\pi) = 5\alpha/(3\cos^2\Theta_W),$$

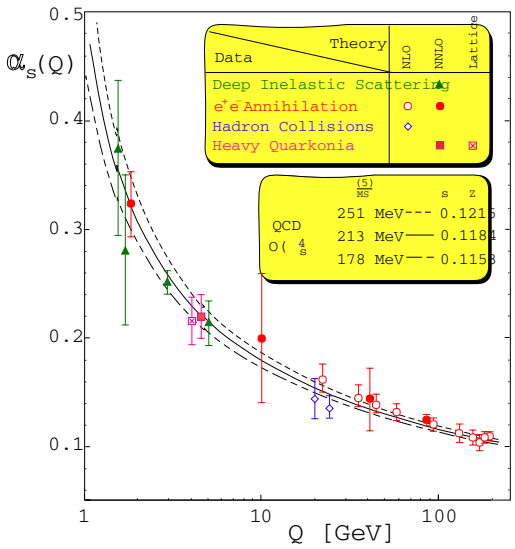

Figure 2.2: Summary of running of the strong coupling α_s [13].

$$\begin{aligned} \alpha_2 &= g^2/(4\pi) = \alpha/\sin^2\Theta_W, \\ \alpha_3 &= g_s^2/(4\pi), \end{aligned} \tag{2.11}$$

where g', g and g_s are the usual $U(1)$, $SU(2)$ and $SU(3)$ coupling constants and α is the fine structure constant.
Assuming that the SM is valid up to the unification scale, one can use the renormalization group equations for the three couplings. In them, a positive contribution (screening) is given by the matter multiplets and a negative one (antiscreening) by the gauge fields. The evolution of the inverse of the couplings as function of the logarithm of energy is shown in fig.(2.3).

We can see that, within the SM, the coupling constants unification at a single point is impossible. This result means that GUT can only be obtained if new physics enters between the electroweak and the Planck scales.

If we try to add to the calculations the new matter and field contents of the minimal SUSY model (see next sections), from the fit requiring unification one finds [fig.(2.3)]

$$M_{SUSY} = 10^{3.4\pm0.9\pm0.4}\ \text{GeV}$$

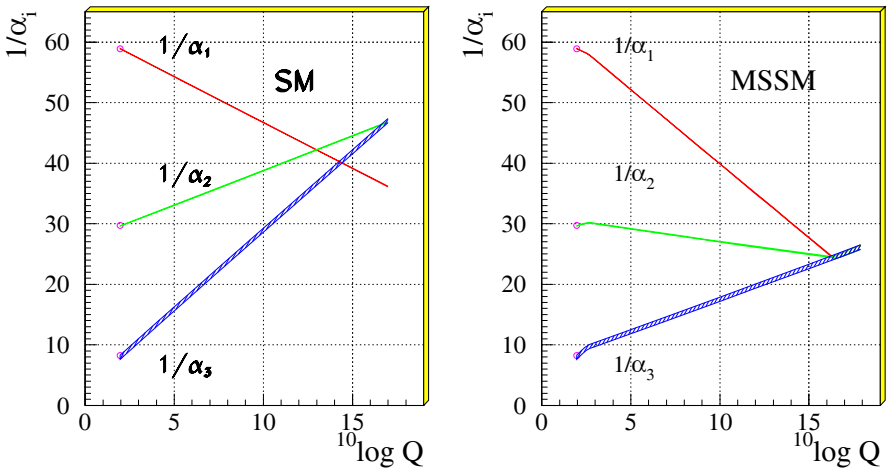

Figure 2.3: Evolution of the inverse of the three coupling constants in the Standard Model (left) and in the supersymmetric extension of the SM (MSSM) (right). Only in the latter case unification is obtained. The SUSY particles are assumed to contribute only above the effective SUSY scale M_{SUSY} of about 1 TeV, which causes a change in the slope in the evolution of couplings. The thickness of the lines represents the error in the coupling constants [14].

$$\begin{aligned} M_{GUT} &= 10^{15.8\pm0.3\pm0.1}\ \text{GeV} \\ \alpha_{GUT}^{-1} &= 26.3 \pm 1.0 \pm 1.0. \end{aligned} \tag{2.12}$$

(The first error originates from the uncertainty in the coupling constants, while the second is due to the uncertainty in the mass splittings between the new particles.)
The SUSY particles are assumed to effectively contribute to the running only for energies above the typical SUSY mass scale M_{SUSY} and they allow a unification point at $\sim 10^{16}$ GeV.

2.3 Solution of the hierarchy problem

Supersymmetry transformations differ from ordinary global transformations as far as they convert bosons into fermions and vice versa. Thus, if we symbolically write SUSY transformations as

$$\delta B = \varepsilon \cdot f,$$

where B and f are boson and fermion fields, respectively, and ε is an infinitesimal transformation parameter, then from the usual (anti)commutation relations for (fermions) bosons

$$\{f, f\} = 0, \quad [B, B] = 0,$$

we immediately find

$$\{\varepsilon, \varepsilon\} = 0.$$

This means that all the generators of SUSY must be fermionic, i.e. they must change the spin by a half-odd amount and change the statistics.

SUSY also implies that the particles of the theory must appear in multiplets, whose members have different spin numbers. In particular, supersymmetry associates known bosons with new fermions and known fermions with new bosons; so the number of existing particles is (at least) doubled, introducing a superpartner to each SM particle.

We can go back to analyse the hierarchy problem in the framework of GUT theory. To get the desired spontaneous breaking pattern, one needs

$$M_H \sim v \sim 10^2 \text{ GeV}, \quad M_\Sigma \sim V \sim 10^{16} \text{ GeV}, \tag{2.13}$$

$$\frac{M_H}{M_\Sigma} \sim 10^{-14} \ll 1,$$

where H and Σ are the Higgs fields responsible for the spontaneous breaking of the $SU(2)$ and the GUT groups.
We consider the radiative correction to the light Higgs mass M_H: it is given

by the Feynman diagram shown in fig.(2.4) and is proportional to the mass squared of the heavy particle. This loop obviously spoils the hierarchy $M_H \ll M_\Sigma$.

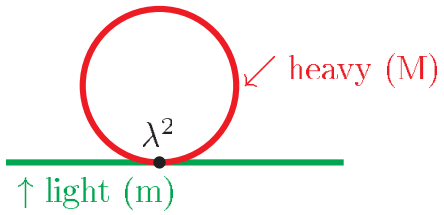

Figure 2.4: Radiative correction to the light Higgs boson mass.

Nevertheless SUSY automatically cancels quadratic corrections. This is due to the existence of superpartners of ordinary particles: the contribution from boson loops cancels those from fermion ones, because of an additional factor -1 coming from the Fermi statistics [fig.(2.5)].

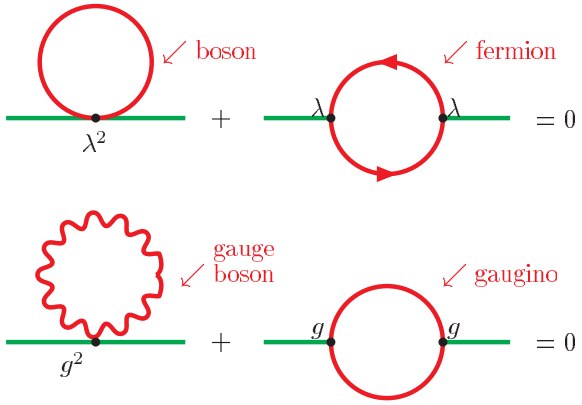

Figure 2.5: Cancellation of quadratic terms.

This cancellation is true in the case of unbroken supersymmetry, being valid the following sum rule for the masses of superpartners:

$$\sum_{bosons} m^2 = \sum_{fermions} m^2. \tag{2.14}$$

Let us take the Higgs boson mass again. Requiring for consistency of perturbation theory that the radiative corrections do not exceed the mass itself gives

$$\delta M_H^2 \sim g^2 M_{SUSY}^2 \sim M_H^2. \tag{2.15}$$

So if $M_H \sim 10^2$ GeV and $g \sim 10^{-1}$, one needs $M_{SUSY} \sim 10^3$ GeV. We get the same rough estimate as from the gauge couplings unification above. Two requirements match together.

That is why it is usually said that supersymmetry solves the hierarchy problem. Moreover, sometimes it is said that: "There is no GUT without SUSY".

2.4 Generalization of the Standard Model: the MSSM

In SUSY theory, the number of bosonic degrees of freedom equals that of fermionic. On the contrary, in the SM one has 28 bosonic and 90 fermionic degrees of freedom (with massless neutrino, otherwise 96). So the SM is highly non-supersymmetric.
Its straightforward extension allowing SUSY requirements is called Minimal Supersymmetric Standard Model (MSSM).

This theory contains all the known fields of the SM and an extra Higgs doublet, together with the partners needed to form supersymmetric multiplets. The interactions are those allowed by the gauge symmetry group $SU_C(3) \otimes SU_L(2) \otimes U_Y(1)$ and by renormalizability. These specifications uniquely determine the MSSM, except the prescription for transformations under the so-called R-parity.

Given an interest in Dark Matter, the most important ingredient is just the realization of R-parity. In terms of its action on the component fields of the theory, this discrete symmetry is $R = (-1)^{3(B-L)+2S}$, where B, L are the baryon and lepton number operators and S is the spin. This means that $R = 1$ for ordinary particles and $R = -1$ for their superpartners.
If R-parity is broken, then there are no special selection rules to prevent the

decay of those supersymmetric particles in the spectrum with masses of order 100 GeV or larger. In particular, the theory would possess no natural candidate for cold DM particles. However, this is only one of the many ills of a theory with broken R-parity: it would also allow baryon- and lepton-number violating interactions, with strengths controlled by the scale of R-parity violation. Therefore, very severe constraints on the violation arise.
We consider only strict R-parity conservation, so that the lightest R-odd particle is stable; this is the so-called Lightest Supersymmetric Particle (LSP).

The particle content of the MSSM is shown in fig.(2.6).

Superfield	Bosons		Fermions		$SU_c(3)$	$SU_L(2)$	$U_Y(1)$
Gauge							
$\mathbf{G^a}$	gluon	g^a	gluino	$\tilde{g}^a$	8	0	0
$\mathbf{V^k}$	Weak W^k	$(W^{\pm}, Z)$	wino, zino $\tilde{w}^k$	$(\tilde{w}^{\pm}, \tilde{z})$	1	3	0
$\mathbf{V'}$	Hypercharge B	(γ)	bino	$\tilde{b}(\tilde{\gamma})$	1	1	0
Matter							
$\mathbf{L_i}$	sleptons	$\tilde{L}_i = (\tilde{\nu}, \tilde{e})_L$	leptons	$L_i = (\nu, e)_L$	1	2	-1
$\mathbf{E_i}$		$\tilde{E}_i = \tilde{e}_R$		$E_i = e_R$	1	1	2
$\mathbf{Q_i}$		$\tilde{Q}_i = (\tilde{u}, \tilde{d})_L$		$Q_i = (u, d)_L$	3	2	1/3
$\mathbf{U_i}$	squarks	$\tilde{U}_i = \tilde{u}_R$	quarks	$U_i = u^c_R$	3^*	1	$-4/3$
$\mathbf{D_i}$		$\tilde{D}_i = \tilde{d}_R$		$D_i = d^c_R$	3^*	1	2/3
Higgs							
$\mathbf{H_1}$	Higgses	H_1	higgsinos	$\tilde{H}_1$	1	2	-1
$\mathbf{H_2}$		H_2		$\tilde{H}_2$	1	2	1

Figure 2.6: Particle content of the MSSM.

The superpartners of the W and charged Higgs bosons, the charged gauginos and higgsinos, carry the same $SU(3) \otimes U(1)$ quantum numbers. Thus, they will in general mix after electroweak symmetry breaking, and the resulting mass eigenstates are linear combinations known as charginos.
The same is true of the superpartners of the photon, Z and neutral Higgs bosons. These fields generally mix to create four mass eigenstates called neutralinos.
The LSP is the lightest neutralino, and we will refer to it as *the* neutralino (χ). It is stable and weakly interacting, thus it is our Dark Matter candidate.

2.5 Dark Matter detection

2.5.1 Relic density

If a new stable particle χ existed, it could have a significant cosmological abundance today. In fact such a particle stays in thermal equilibrium in the early Universe, when the temperature exceeds its mass m_χ. The equilibrium abundance is maintained by annihilation with its antiparticle $\bar{\chi}$ into lighter particles l ($\chi\bar{\chi} \to l\bar{l}$) and vice versa ($l\bar{l} \to \chi\bar{\chi}$). In our case, χ is a Majorana particle: $\chi = \bar{\chi}$.
As the Universe cools to a temperature less than m_χ, the equilibrium abundance drops exponentially; when the rate for the annihilation reaction ($\chi\bar{\chi} \to l\bar{l}$) falls below the expansion rate H, the interactions "freeze out" and a relic cosmological abundance remains.

More quantitatively, the χ equilibrium number density is

$$n_\chi^{eq} = \frac{g}{(2\pi)^3} \int f(\mathbf{p}) d^3\mathbf{p}, \tag{2.16}$$

where g is the number of internal degrees of freedom (i.e. the number of helicity states) of the particle and $f(\mathbf{p})$ is the Fermi-Dirac or Bose-Einstein distribution. At $T \ll m_\chi$, $n_\chi^{eq} \simeq g(m_\chi T/2\pi)^{3/2}\exp(-m_\chi/T)$, so that the density is suppressed.
In particular, shortly after T drops below m_χ, the annihilation rate $\Gamma = \langle\sigma_A v\rangle n_\chi$ ($\langle\sigma_A v\rangle$ is the thermally averaged total cross section for $\chi\bar{\chi}$ into lighter particles times the relative velocity v) becomes smaller than H and χs fall out of equilibrium.
The evolution of their number density $n_\chi(t)$ is analytically described by the Boltzmann equation:

$$\frac{dn_\chi}{dt} + 3Hn_\chi = -\langle\sigma_A v\rangle \Big[(n_\chi)^2 - (n_\chi^{eq})^2\Big]. \tag{2.17}$$

The second term on the left-hand side accounts for the expansion of the Universe. The right-hand side vanishes at equilibrium, when we find $n_\chi \propto a^{-3}$:

the density decreases with the scale factor of expanding Universe. More precisely, the first term into brackets arises from depletion of χs due to annihilation, while the second term accounts for creation from the inverse reaction. Once eq.(2.17) is numerically solved, it allows us to write the contribution of χ to the energy density of the Universe as

$$\Omega_\chi = \frac{m_\chi n_\chi}{\rho_c} \simeq \frac{3 \cdot 10^{-27} cm^3 s^{-1}}{\langle \sigma_A v \rangle} \, h^{-2}.$$

Our hypothesis to solve the DM problem within the SUSY frame can be summarized as follows: the WIMP neutralinos created in the Big Bang decoupled from ordinary particles at the temperature of SUSY symmetry breaking ($\sim$ 1 TeV). They began to arrange themselves in structures, due to gravity, forming the future galactic halos. Then, after baryons decoupled from radiation ($\sim$ 0.25 eV), they were attracted into the cold DM objects to build up the galaxies.

2.5.2 Direct Dark Matter search

If the halo of the Milky Way consisted of WIMP neutralinos, then a large number of them should pass through every square centimeter of the Earth's surface each second. The most satisfying proof of the WIMP hypothesis would be direct detection of these particles, by observation of nuclear recoil after WIMP-nucleus elastic scattering.
The cross section of this process depends on the SUSY model, but is clearly very low and makes the interactions rare. However specialized detectors could reveal the tiny energy deposited by the very occasional WIMP-nucleus scattering. The maximum energy transfer is given by

$$E_r = \frac{\mu^2 v^2}{m_N}(1 - \cos\theta), \qquad \mu = \frac{M_W m_N}{M_W + m_N}$$

(E_r: recoil energy; v: WIMP velocity < 500 km/s $\sim$ galactic escape velocity; M_W: WIMP mass; m_N: nucleus mass).
The detector must be sensitive to energy releases of the order of 10 keV,

observable through different techniques such as temperature increase in cryogenic apparatus, ionization or scintillation. The hardest point is separating the signal - expected with a rate of one event per day per 10 kg of detector mass - from the millions of background events, generated by cosmic rays and radioactivity. For this reason, it is customary to look for an annual modulation of the signal: considering the rotation of the Earth aroud the Sun, the WIMP flux should be greater in June (when the rotation velocity sums up to that of the Solar System with respect to the galaxy) than in December (when the two velocities are opposite).
Two of the most known experiments which tried to detect DM directly are DAMA [6] and CDMS [7]. Their results are shown in fig.(2.7).

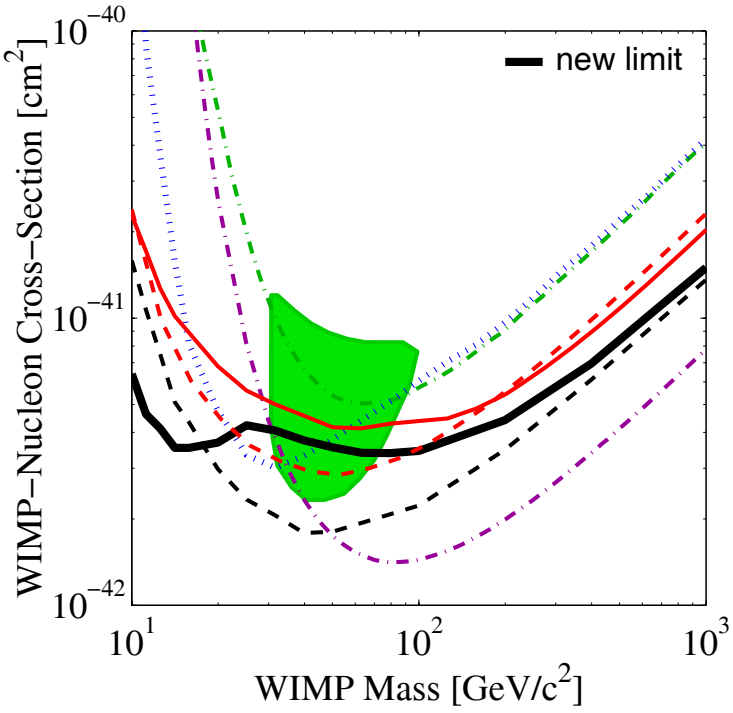

Figure 2.7: The region above the black curve is excluded at 90% C.L. by CDMS. The green shaded region is the DAMA 3σ allowed region.

2.5.3 Indirect Dark Matter search

We have seen that if WIMP neutralinos build the Dark Matter in the galactic halo, the ones with an orbit passing through a celestial body will have a small but finite probability of scattering from a nucleus therein. In doing so, they could scatter to a velocity smaller than the escape one and become gravitationally bound to the body. Once captured, additional scatters settle them to the core; in such a way neutralinos could have accumulated in the centre of the Sun and of the Earth.
This picture allows an indirect detection method for neutralinos, looking at their annihilation products. In fact, WIMP which have accumulated as explained above can annihilate into ordinary particles such as quarks and leptons, and - if heavy enough - to gauge and Higgs bosons. The majority of the annihilation products are absorbed almost immediately, but some of them decay and produce neutrinos, which can pass through the celestial body and be detected by *neutrino telescopes*.
Considering the different channels, the typical neutrino energy is roughly $\frac{1}{3}$ to $\frac{1}{2}$ the WIMP mass, far from the solar neutrino energies. A neutrino signal in the direction of the centre of the Sun or of the Earth, with energy in the range of 10 GeV to few TeV, is a good experimental signature for Dark Matter.

Quantitatively, the neutrino flux from neutralino annihilations depends on the details of the interaction-decay-propagation chain. It is fundamental to consider also the capture versus the annihilation balance in the core of the celestial body. The differential neutrino flux is given by

$$\frac{d\Phi}{dE} = \frac{\Gamma_A}{4\pi D^2} \sum_f B_\chi^f \Big(\frac{dN_\nu}{dE}\Big)_f, \tag{2.18}$$

where Γ_A is the annihilation rate, D is the distance from the source, f is the neutralino pair annihilation final state and B_χ^f its branching ratio; $\left(\frac{dN_\nu}{dE}\right)_f$ is the differential energy spectrum of neutrinos at the surface of the Sun or Earth, expected from channel f. Determination of these spectra is complicated as it involves hadronization of the annihilation products, interaction

of particles with the surrounding medium and the subsequent interaction of neutrinos with it. For this reason, the spectra of neutrinos from the Sun are different from those from the Earth.

It is also necessary to compute the annihilation rate Γ_A, through a parametrisation of the χ density in the core region. The equation that describes the time variation of the number of χs is

$$\frac{dN_\chi}{dt} = R_C - R_A N_\chi^2, \tag{2.19}$$

where R_C is the caption rate and R_A is defined by $\Gamma_A = \frac{1}{2} R_A N_\chi^2$ (the 1/2 factor accounts fro the vanishing of two χs in a single annihilation). Solving eq.(2.19) for Γ_A gives

$$\Gamma_A = \frac{R_C}{2} \tanh^2\Big(\frac{t}{\tau}\Big), \tag{2.20}$$

in which $\tau = 1/\sqrt{R_C R_A}$ is the equilibrium time scale.

Other difficulties arise now from the evaluation of the capture rate. Some assumptions about SUSY parameters are needed, which can give macroscopic differences in the resulting neutrino flux and then in the signal expected by a neutrino telescope.

Chapter 3

The ANTARES experiment

The ANTARES (Astronomy with a Neutrino Telescope and Abyss environmental RESearch) Collaboration is building a neutrino underwater telescope, to be deployed at a depth of 2500 m in the Mediterranean sea, near the Southern French coast.
The experiment aims to detect neutrinos with energies above 10 GeV, using the Cherenkov light emitted in sea water by charged particles, which are produced in neutrino interactions.

3.1 Neutrino Astronomy

Most of our current knowledge of the Universe comes from the observation of photons: as cosmic information carriers, they are stable and electrically neutral; they are easy to detect over a wide energy range and their spectrum gives information about the physical properties of the source. Unfortunately the hot, dense regions which form the central engines of stars, active galactic nuclei (AGN) and other astrophysical sources are completely opaque to photons, and therefore they can not be investigated by direct photons observation.
Moreover, high energy photons interact with the Cosmic Microwave Background to create electron-positron pairs; this is the Greisen-Zatsepin-Kuz'min effect (GZK), which suppresses any possibility of surveying the sky over dis-

tances greater than 100 Mpc with high energy (>10 TeV) gamma rays.

In order to observe the inner workings of the astrophysical objects and to obtain a description of the Universe over a larger range of energies, we need a probe which is electrically neutral - so that its trajectory will not be affected by magnetic fields - stable and weakly interacting, so that it will penetrate regions which are opaque to photons. The only candidate currently known is the neutrino.

Nuclear fusion in the core of stars and Supernova explosions are known astrophysical phenomena producing neutrinos, but high energy (>10 GeV) neutrino sources have not been observed yet. However, their existence can be inferred from the properties of cosmic rays.
Primary cosmic rays are protons and - in a small fraction - heavier nuclei. Their energy spectrum is a power law which extends to the recently observed value of 10^{20} eV. Protons themselves have limited use as astrophysical information carriers: being deflected by cosmic magnetic fields, their sources are unknown, although Supernova remnants and AGN have been proposed. Whatever the source, it is clear that accelerating protons to such high energies is likely to generate a large associated flux of photo-produced pions, which decay to yields gamma rays and neutrinos.
We also recall that a good theoretical candidate to explain the non-luminous, non-baryonic major content of matter in the Universe is the WIMP neutralino. Neutrino telescopes are not directly sensitive to WIMPS, but they may detect high energy neutrinos produced by the decay of gauge bosons and heavy particles from $\chi - \chi$ annihilation.

The detection of a relic cosmological population of supersymmetric particles would be of immense importance to both cosmology and particle physics; furthermore the existence of very high energy cosmic-ray protons implies the existence of high energy neutrinos. These are the key reasons to investigate the new field of *neutrino astronomy*.
The drawback is that the weak interactions of neutrinos require a very massive detector, with extremely good background rejection, to observe a measurable flux.

3.2 Detection principle

Neutrinos are detected through their interaction with a nucleon N, via either charged current ($\nu_l + N \rightarrow l + X$) or neutral current ($\nu_l + N \rightarrow \nu_l + X$) weak interactions. The experimental signature depends on the type of reaction and on the neutrino flavour. In this thesis the focus is on muon neutrinos, which are the most interesting in a search for point sources.

Since the Earth acts as a shield against all particles except neutrinos, a neutrino telescope uses the detection of upward-going muons as a signature of a ν_μ interaction in the matter below the detector. It is required to discriminate between upward-going muons against the much higher flux of downward-going atmospheric muons [fig.(3.1)]. For this reason, the detector should be installed in a deep site, where a layer of matter would shield it.

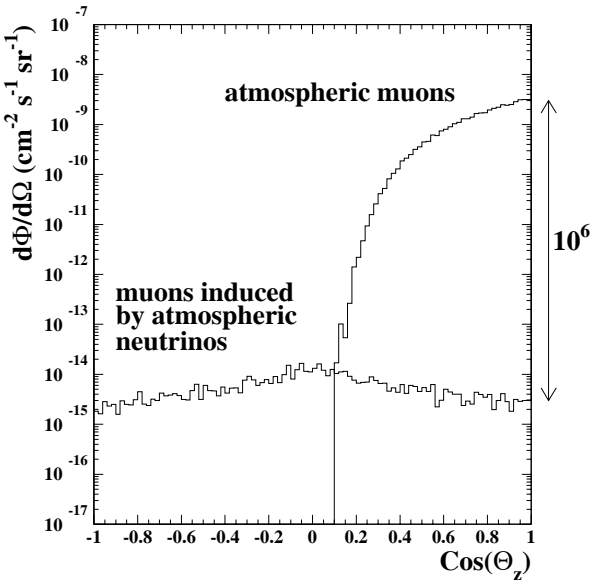

Figure 3.1: Zenith angular distribution of the muon flux above 1 TeV from atmospheric muons and atmospheric neutrino induced muons at 2300 m water equivalent depth.

The muon detection medium may be water or ice, through which the muon emits Cherenkov light. The Cherenkov angle θ is related to the particle

velocity β and the refractive index of the medium n:

$$\cos\theta = \frac{1}{n\beta}. \tag{3.1}$$

In the energy range interesting for ANTARES (E>10 GeV), particles will be ultra-relativistic ($\beta = 1$). The refractive index of sea water is $n = 1.35$ for a wavelength of 450 nm, therefore the Cherenkov light is emitted under 42° for this wavelength. This easy geometrical pattern of light emission allows a precise reconstruction of tracks from the measurement of only few hits at different space points.

The number of photons produced along a flight path dx, in a wave length bin $d\lambda$, for a particle carrying unit charge is

$$\frac{d^2N}{d\lambda dx} = \frac{2\pi\alpha}{\lambda^2}\sin^2\theta. \tag{3.2}$$

At wavelengths of 400-500 nm, the efficiency of photomultipliers tubes, as well as the transparency of water are maximal. Within 1 cm flight path, 100 photons are emitted in this wavelength bin. At a perpendicular distance of 40 m from a charged track, the density of photons between 400-500 nm is still 1 per 340 cm^2, neglecting absorption and scattering effects. This gives an indication of the active detector volume around each photomultiplier that is used in ANTARES to detect Cherenkov light.

The transmission of light in water is parameterised by the absorption length λ_a, the scattering length λ_s and the scattering function $f(\theta)$, which describes the angular distribution of the scattering. Measurements performed at the ANTARES site give λ_a in the range 25÷55 m and λ_s in the range 120÷300 m, from UV to blue light (370÷470 nm). The scattering function is peaked in the forward direction, with an average value for the cosine of the scattering angle $\langle\cos(\theta)\rangle \simeq 0.9$.

3.3 The ANTARES detector

The ANTARES detector is currently under construction and will be deployed in a site near Toulon - 42°50' Northern latitude and 6°10' Eastern longitude -

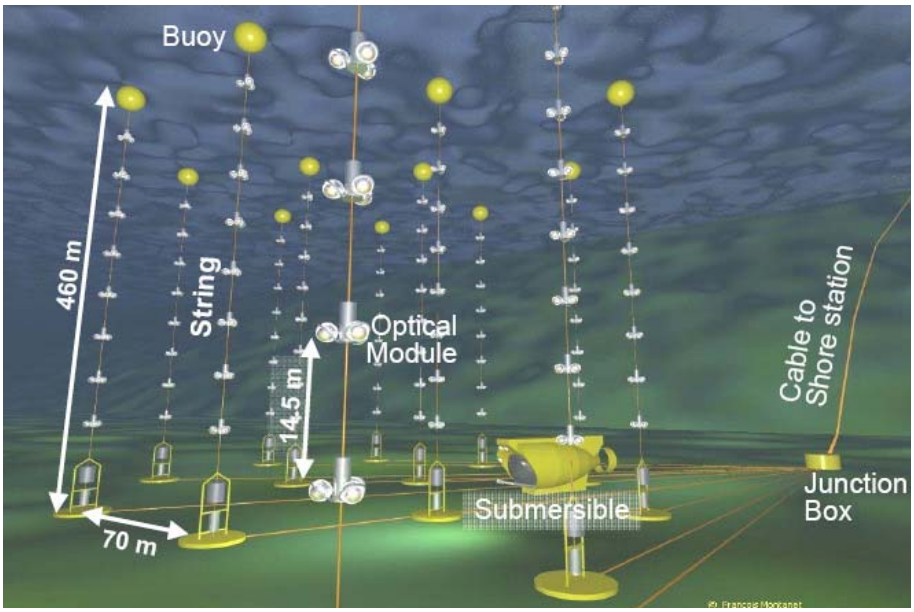

Figure 3.2: Artist's view of the ANTARES detector.

at a depth of ∼2500 m under the sea level. An artist's view of the apparatus is shown in fig.(3.2).

In ANTARES the Cherenkov light is detected by a 3D-array of 900 optical modules (OMs): pressure resistant glass spheres containing photomultipliers tubes (PMTs). The OMs are grouped in triplets - called storeys - and arranged in 12 lines, each containing 25 storeys, on a surface of about 0.05 Km^2. The position of the strings on the seabed is shown in fig.(3.3).

A junction box distributes the power and clock synchronization signals to the lines and collects the data output; it is connected to the shore by a 42 km electro-optical cable. The lines are kept straight by the floating force of a buoy at the top and an anchor at the bottom; the 25 storeys are spaced by 14.5 m, starting from 100 m from the sea floor. All the PMTs are 10" wide and 45° downward looking. The electronics boards are inside titanium cylinders, positioned at the centre of each storey; the whole device is called Local Control Module (LCM). Every LCM controls three OMs.

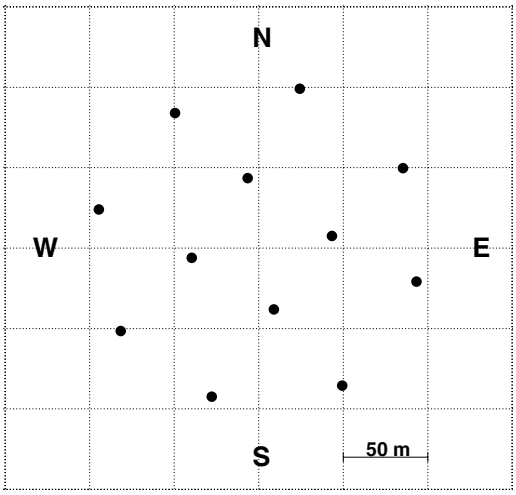

Figure 3.3: Position of the strings on the seabed.

The readout of each PMT is shared by two Analog Ring Sampler (ARS) chips, which provide the digitization of the analog signal of time and charge. Thus every LCM contains 6 ARSs. Two ARSs per PMT are needed to avoid the dead time ($\sim$ 80 ns) induced by signal sampling: the first ARS holds the "even" events, the second the "odd" events. Photon arrival times, PMT charge amplitudes and positions allow the reconstruction of the tracks and the estimate of their energy. All the data collected through the ARSs are sent to the shore station; with a noise rate of 70 kHz, a flow of about 1 GB/s is produced. A trigger software (see Chapter 5), running on a PC farm, performs an online filtering and reduces the data rate by at least a factor 100.

3.3.1 Effective volume and effective area

The performance of the ANTARES detector can be defined in terms of two quantities, independent of any neutrino flux model:

- Effective volume: the volume of a 100% efficient detector to observe neutrinos, which would obtain the same event rate as ANTARES for a

given neutrino interaction rate;

- Effective area: the area of a 100% efficient surface for detecting through-going neutrinos, which would observe the same event rate as ANTARES for a given neutrino flux.

Given a MC sample, the effective volume can be computed as

$$V_{eff}(E_\nu) = \frac{N_{selected}(E_\nu)}{N_{generated}(E_\nu)} \times V_{can}. \tag{3.3}$$

The so-called *can* volume (V_{can}) is built increasing the dimensions of the instrumented volume by three absorption lenghts. Photons produced by muons out of the can are assumed not to reach the detector.
Using eq.(3.3) and a neutrino flux ϕ_ν, the neutrino interaction rate per unit volume is

$$R_{observed} = \int V_{eff}(E_\nu)\,(\rho N_A)\,\sigma(E_\nu)\,\frac{d\phi_\nu}{dE_\nu}\,dE_\nu, \tag{3.4}$$

where ρ is the target density and N_A the Avogadro's number.
From eq.(3.4) above, we can combine $V_{eff}(E_\nu)$, (ρN_A) and $\sigma(E_\nu)$ to reproduce a quantity which, when multiplied by a differential neutrino flux and integrated, gives a rate of observed events. Multiplying the three terms by the probability of transmission through the Earth, P_{Earth}, we get the effective area for neutrinos reaching the detector from the opposite surface of the Earth:

$$A_{eff} = V_{eff}(E_\nu) \times (\rho N_A) \times \sigma(E_\nu) \times P_{Earth}(E_\nu). \tag{3.5}$$

The quantities defined in eqs.(3.3) and (3.5) are fundamental to compare the performances of different trigger and track reconstruction techniques, as it will be shown in Chapter 6.

3.3.2 Angular resolution

The angular resolution of the detector depends on the neutrino energy: high energy neutrinos produce energetic muons, which are easier to reconstruct because of the big amount of Cherenkov light emitted. Furthermore, the

lower the neutrino energy is, the bigger the scattering angle between neutrino and muon, and then the uncertainty on the neutrino direction.
To characterize the pointing accuracy of the detector, the median of the distribution of angle reconstruction error is used. The resolution thus obtained is shown in fig.(3.4). At the highest energy, the angular resolution is smaller

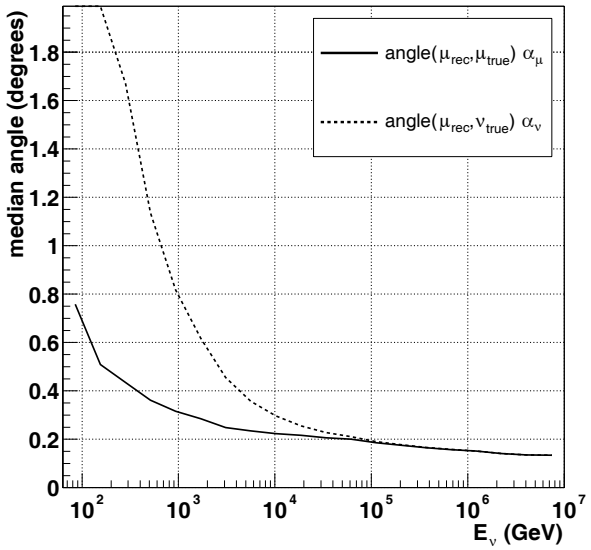

Figure 3.4: Angular resolution of the detector as a function of the neutrino energy. Both the angles of the reconstructed muon w.r.t. the true muon (α_μ) and of the reconstructed muon w.r.t. the neutrino direction (α_ν) are considered.

then 0.2° and is limited by the accuracy of the muon reconstruction. Below about 10 TeV, the resolution on the neutrino direction is dominated by the scattering angle; this unpleasant feature will be dealt with in Chapter 6.

3.3.3 Energy response

The energy response is determined by the energy fraction transferred to the muon in the neutrino interaction, the energy lost by the muon outside the detector and the energy resolution of the detector.

The muon energy determination requires different techniques in different energy ranges.
Below 100 GeV, the muons are close to minimum-ionizing, and the energy of contained events, with start and end points measured inside the detector, can be determined accurately from the range.
Above 100 GeV, the range cannot be measured because of the limited size of the detector, but the visible range determines a minimum energy that can be used for the analysis of partially-contained events: starting events in which the vertex point is measured inside the detector, and stopping events in which the endpoint is measured.
Above 1 TeV, stochastic processes (bremsstrahlung, pair production, δ-rays) are dominant, and the muon energy loss becomes proportional to the energy. The detection efficiency also increases with energy, because of the additional energy loss. Monte Carlo studies have shown that the neutrino energy can be determined within a factor 3 above 1 TeV.
Above 1 PeV, the Earth becomes opaque to upward-going vertical neutrinos. Events with these energies are accessible only if induced by neutrinos close to the horizon.

3.3.4 Observable sky

The ANTARES neutrino telescope, situated at a latitude of $\sim 43^\circ$ North, can observe upward-going neutrinos from most of the sky (about 3.5π sr), due to the rotation of the Earth. Declinations below -47° are always visible, while those above $+47^\circ$ are always precluded [(fig.(3.5)]. Declinations between -47° and $+47^\circ$ are visible for part of the sidereal day, the Galactic Centre for most of it.

3.3.5 Optical background

Since the beginning, several measurements of the optical background have been performed at different depths at the ANTARES site. These results have been summarized in a large number of internal reports. A precise character-

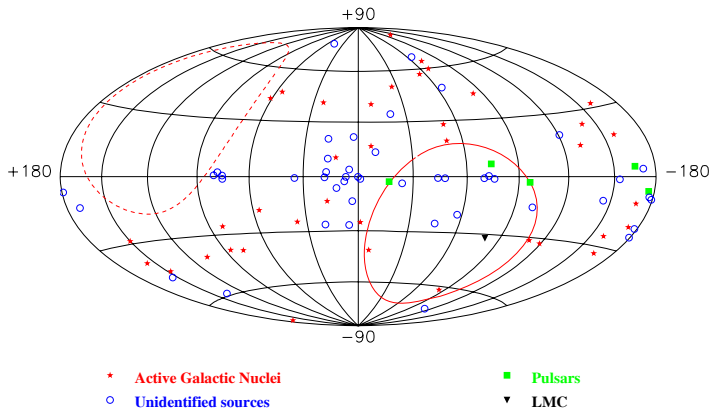

Figure 3.5: Visible sky in Galactic coordinates for ANTARES. The area within the dashed line is not observable, while the area within the solid line is observable 24 h a day. The sources shown are from the EGRET catalogue.

ization of the optical background is in fact necessary to optimize the choice of the detector trigger and to avoid dead time in data taking.

During the tests, the OMs have been arranged in different setups, usually keeping at least one close pair to study coincidences and correlations.
In fig.(3.6) we show an example of a time stream registered by an OM.
Two different components can be identified:

1. a continuous background, whose frequency varies slowly over periods of several hours and usually corresponds to several tens of kHz;

2. some sharp peaks, ranging up to tens of MHz and lasting few seconds.

In order to quantify the optical background, two definitions were introduced: the *continuous component* is the lower envelope of the plot, representing the counting rate of a given OM as function of time; the *burst activity* corresponds to a counting rate higher than 120% the continuous component, which may generate in the PMTs a dead time, lasting up to many seconds [fig.(3.8)].

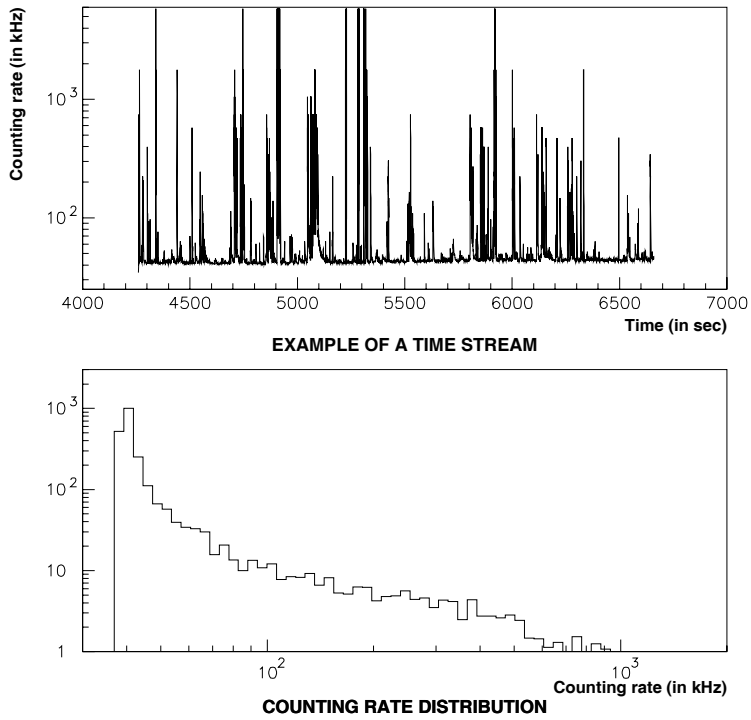

Figure 3.6: Top panel: example of a time stream recorded during a test in 1998. Bottom panel: distribution of the counting rates for the above time stream.

The background light is known to be caused by the radioactive decay of ^{40}K isotope, naturally present in the sea salt, and bioluminescent living organisms. ^{40}K has two major decay branches:

- β^- decay with 89.3% probability and a kinetic endpoint energy of $Q =$ 1.311 MeV;
- electron capture with 10.7% probability, followed by a γ emission of E_γ = 1.46 MeV.

The electrons produced travel on average 2.3 mm and do not produce secondary (shower) particles above Cherenkov threshold; the γs travel on average 68 cm and produce about two Compton electrons above Cherenkov threshold.

The level of the continuous component is strongly related to ^{40}K decay rate: simulations [15] taking into account the salt content of the sea at the ANTARES site give an expected counting frequency of about 30 kHz for a PMT. However, since the water salinity was measured to be approximately constant, the baseline variations - ranging from about 50 to 150 kHz and registered over long time periods (days or months) - must be due to another contribution.
Fig.(3.7) shows the correlation in time between the continuous component and the registered current speed.

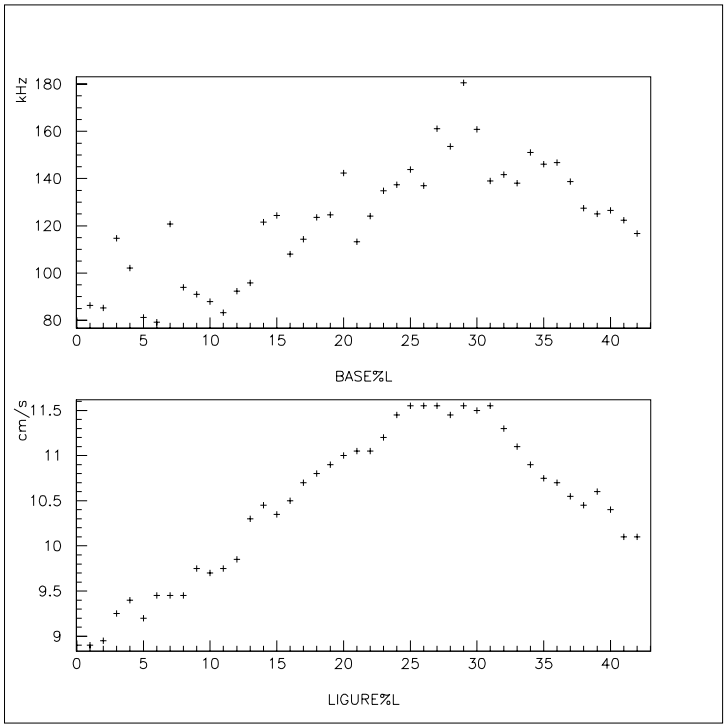

Figure 3.7: Top curve: evolution of the baseline. Bottom curve: evolution of current speed. Both are on the same time scale (total: 21h).

The excess observed over the expected ^{40}K rate is therefore probably caused by a slightly variable bioluminescence activity, due for example to a larger

number of bacteria carried near the OMs.

Also the bursts can be explained as an organic signal: many organisms living in sea depths emit light continuously, but they also produce flashes of duration varying from about 0.1 s to tens of seconds. Even the total number of photons emitted in a burst may vary from 10^8 to 10^{12} [16].

In fig.(3.8) we show the counting rate of six ARSs - belonging to a triplet of OMs taking data contemporarily - as a function of time.

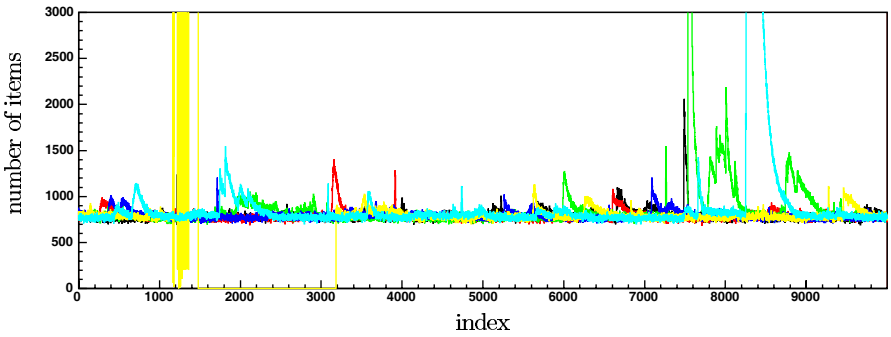

Figure 3.8: Count rate of six ARSs (belonging to a triplet of OMs) as a function of time: index 1000 corresponds to 13 s.

It can be noticed that the bioluminescence bursts appear to be uncorrelated between the different OMs. There is also a dead time (called XOff) for one of the ARSs, between index value 1400 and 3200. Indeed, when the background rate exceeds several hundreds of kHz, buffers of the ARSs fill up to their maximum capacity; in this case, data are no longer recorded until the buffer are emptyed.

Chapter 4

Analysis of MILOM data[1]

4.1 The MILOM line

The MILOM (Mini Instrumentation Line with Optical Modules) is a prototype line deployed at the ANTARES site in March 2005. Its aim is a measurement of the ambient parameters (water current, salinity, temperature, optical attenuation length, ...), a check of the electronics in situ and a verification of the acoustic position system.
A schematic drawing of the MILOM is shown in fig.(4.1) [17]. The line contains three storeys, equipped with the following devices.
Top storey:

- Optical Module;
- Current Profiler (ADCP);
- Led Optical Beacon;
- Spy Hydrophone.

Middle storey:

- 3 Optical Modules;

[1]The content of this chapter appeared in the internal note N. Cottini: *Background measurements with MILOM*, ANTARES-Phys/2006-002.

- GEMISEA sound velocimeter.

Bottom storey:

- Conductivity-Temperature probe;
- C_STAR light transmissiometer;
- Led Optical Beacon;
- Acoustic Positioning Module with a hydrophone.

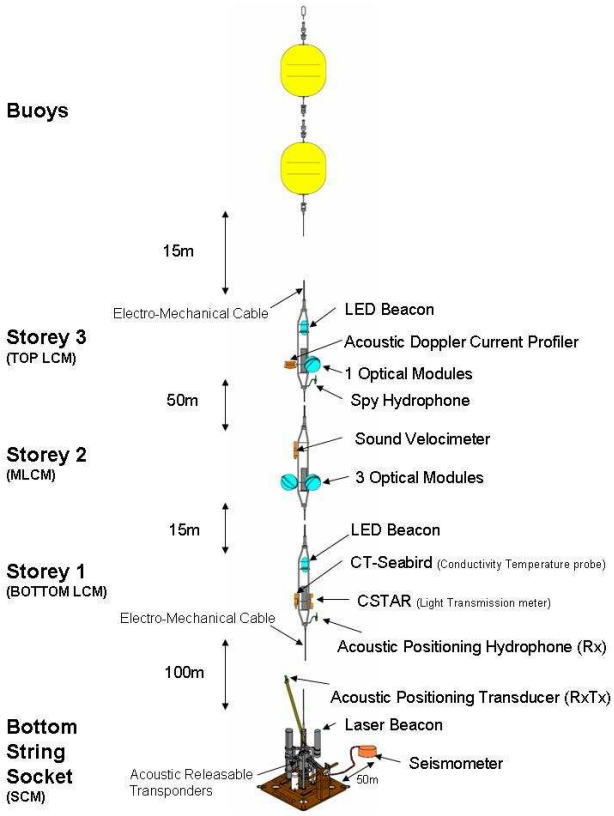

Figure 4.1: MILOM scheme.

The distance between the top and the middle storey is 50 m, between the middle and the bottom is 14.5 m. The BSS is located 100 m below and is equipped with a Laser Beacon, a Seismometer, an Acoustic Positioning Module with a transducer and a pressure sensor.

4.2 Background measurement with MILOM

The MILOM line allowed the Collaboration to verify the Data Acquisition system and to monitor over a long period the optical background from ^{40}K decay and bioluminescence. This information will be used later in this work, when adding this kind of random background signal to a sample of pure physics events, generated by the ANTARES MonteCarlo; this is a fundamental step for a realistic data analysis.

The data taking started in the spring of 2005 and is still going on. The entire electronic system has been very stable over this period.
Before the summer the bioluminescence rate was high, but since the beginning of July it has dropped to 60-70 kHz. Fig.(4.2) shows the rates for the three optical modules in the MILOM middle storey up to December 2005.

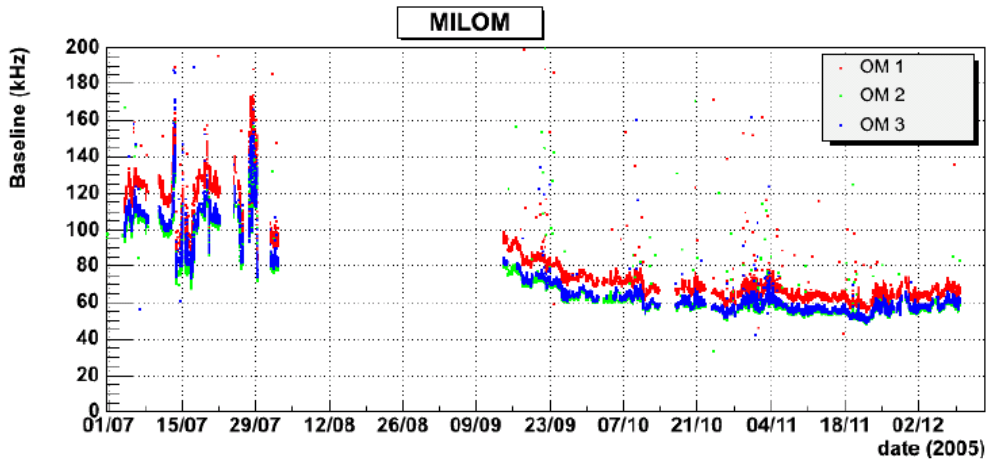

Figure 4.2: Baseline counting rate from the three optical modules in MILOM middle storey, between July and December 2005.

4.2.1 Time intervals between consecutive hits from each ARS

The rates shown in fig.(4.2) are computed using the number of events recorded and the time span of the particular data taking run.
We have tried to reproduce these results, using the statistical properties of the background hits recorded.

We have analysed the distribution of time differences between a hit and the previous one registered by a single ARS of the middle storey [fig.(4.3)-(4.4)]. In the particular instance here considered, we have used a MILOM data file recorded on 30 September 2005 and stored at the Antares database in Lyon.
We assume that both ^{40}K and bioluminescence generate events randomly in time, according to Poisson distributions with different mean values μ_A and μ_B; so the whole background source can be described using a Poisson distribution with $\mu = \mu_A + \mu_B$.
We also consider that each ARS registers (in an alternative manner) half of the signals given by a PMT. Thus we do not fit the histograms of time differences using an exponential, but a Gamma distribution

$$f(t;\lambda,k) = \frac{t^{k-1}\lambda^k e^{-\lambda t}}{\Gamma(k)}, \quad 0 < t < \infty. \tag{4.1}$$

k defines a sort of event spacing: it is set to 2 to specify that, given for instance three events, the chosen ARS registers the first, neglects the second and registers again the third. The mean value of the distribution is given by $\overline{t} = \frac{k}{\lambda}$. Some examples of the data and the fits obtained are shown in figs.(4.3) and (4.4).

The rate R of the background signal on a PMT can be estimated as $R = 2 \cdot (\frac{1}{\overline{t}})$. The values obtained for each ARS are shown in the next table (the error is negligible, due to the error on the fit parameter).

ARS	0	1	2	3	4	5
Rate (kHz)	88.94	89.03	75.11	75.09	75.18	75.19

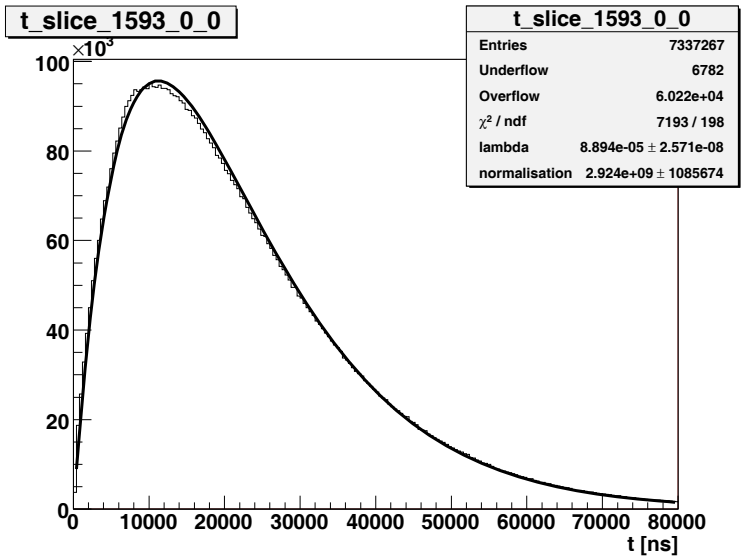

Figure 4.3: Distribution of time differences between a hit and the previous one registered by the ARS 0 of the MILOM middle storey.

It should be noticed that the χ^2/ndf value is always very large, so the model chosen does not seem to fit the data.
One might be tempted to attribute this behaviour to electronic readout errors. It has indeed been observed that ARS chips sometimes show a problem (known as *bit-flip*) in data digitization: in the sequence of bits holding the time information, a 0 bit is read as a 1 or vice versa.
This could cause - in our case - meaningless time differences between hits, or even negative ones: given two hits on a single ARS, the time counter associated to the second could be smaller than that of the first, even if the second hit has clearly been registered later.
In the statistical box of our histograms [fig.(4.3)-(4.4)], we can read the number of underflows, that is the number of negative time differences. We also show in fig.(4.5), the sum of the histograms for all the ARSs of the middle storey, using an axis symmetric around 0. Here the number of negative time differences is 405 over $3 \cdot 10^7$ entries. Given the tiny size of the effect, one may assume that this can not be the cause of the anomalous behaviour.

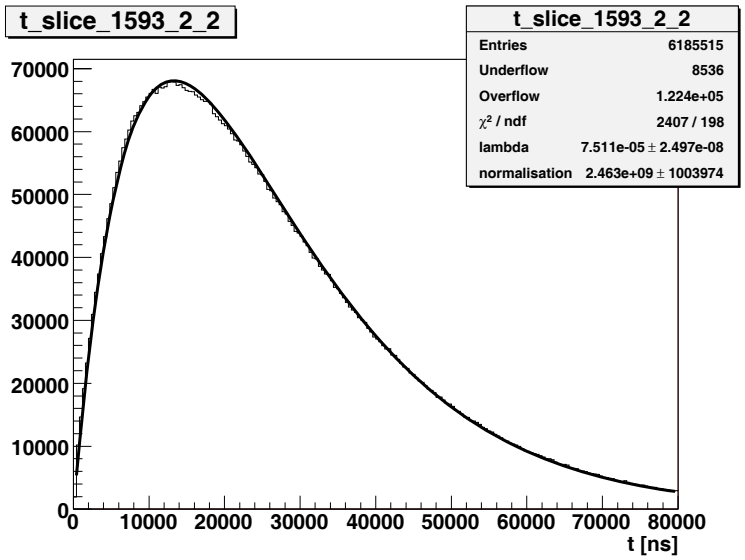

Figure 4.4: Distribution of time differences between a hit and the previous one registered by the ARS 2 of the MILOM middle storey.

Alternatively the disagreement with Gamma distribution might be explained if bioluminescence can not be described as a random process, like ^{40}K decay. To investigate this possibility, we consider the number of events recorded in a so-called TimeSlice, that is in a time interval of 13 ms. Fig.(4.6) shows an example referring to the data (up to TimeSlice number 1900) from ARS 1 and ARS 4 respectively.

We can clearly identify the continuos component of the background, from which we can estimate a rate consistent with the values previously found through the fit. Furthermore, we notice some small bursts - which do not increase the counting rate up to MHz, but only by 50% or less.

Thus, the model we chose can be considered only a reasonable approximation of the true behaviour of bioluminescence, which reveals properties not stationary in time, even excluding big bursts.

We have repeated our analysis fitting with Gamma distributions the data registered in different days of the second half of 2005. The resulting rates

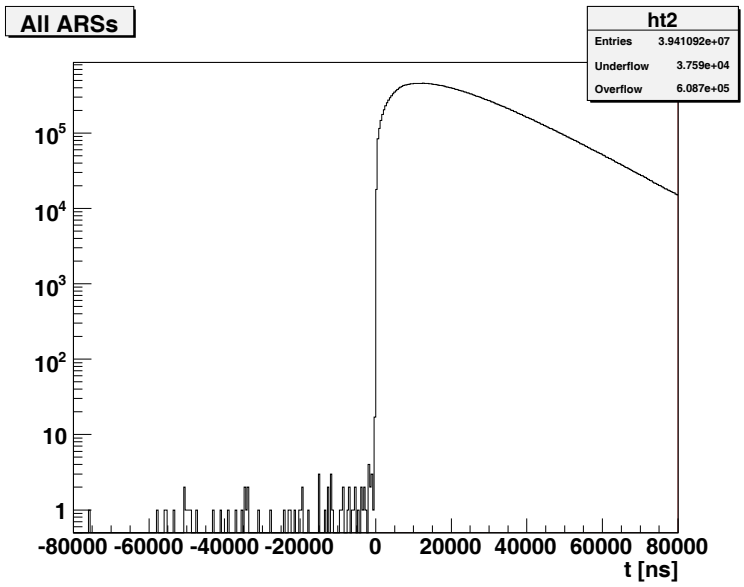

Figure 4.5: Sum of the histograms of fig.(4.3) up to fig.(4.4), with the x axis extended to negative values.

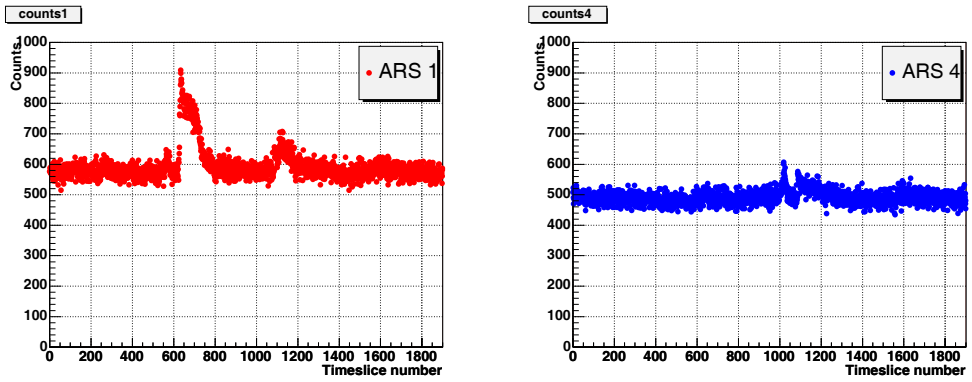

(a) (b)

Figure 4.6: (a) Number of events recorded by ARS 1 per TimeSlice. (b) Number of events recorded by ARS 4 per TimeSlice.

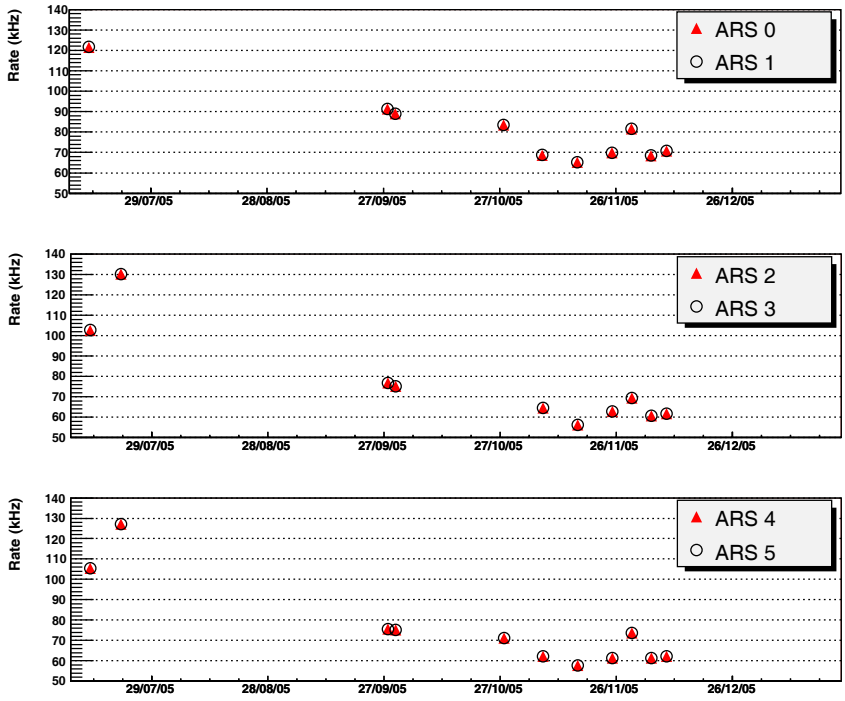

Figure 4.7: Rates recorded by the ARSs of the MILOM middle storey between July and December 2005. Each plot refers to the pair of ARSs associated to each individual PMT, as indicated. In the long empty period, the MILOM was unavailable.

obtained are shown in fig.(4.7): a plot is present for every OM of the middle storey, from which we can see that the two ARSs associated with each PMT register roughly the same rate.

We show the output of our analysis, performed over the entire data taking period, in fig.(4.8). The rates obtained are consistent with the official ones of fig.(4.2). We notice the same decrease of counting rates with time and also the higher counts of OM 1 compared to the others.

Despite the problems mentioned above, the result seems promising.

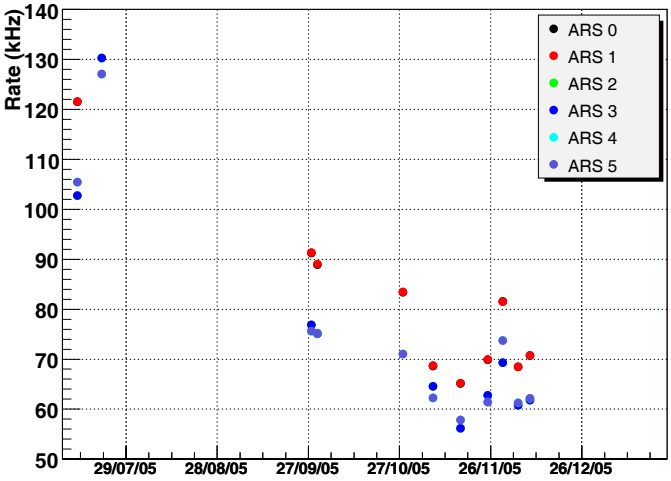

Figure 4.8: Rates recorded by the ARSs of the MILOM middle storey between July and December 2005. In the long empty period, the MILOM was unavailable.

4.2.2 Coincidence events and clock offsets

We now turn to the analysis of the so-called coincidence events, that is to say background events registered by a pair of PMTs. This interesting point was first drawn from MonteCarlo simulations [15] of the light signal generated by a single ^{40}K decay and registered by two OMs, belonging to the same storey.

We choose an appropriate time window, 100 ns wide, centered around 0 ns. We select a pair of PMTs, implying four data series from the four ARSs involved.

If we take into account, for instance, PMT 1 and PMT 2, we have to look for coincidences in the matched data series of ARS0-ARS2, ARS0-ARS3, ARS1-ARS2, ARS1-ARS3.

For each combination, we compute the time differences between a hit from the first ARS and the hit - if present - from the second ARS, not further in time than half of the time window width. We get a flat distribution, determined by differences which randomly happen to fall within the window,

and a Gaussian peak given by genuine coincidences.

The distributions obtained for the three possible PMT pairs, using a MILOM run registered on 7 November 2005, are shown in fig.(4.9).

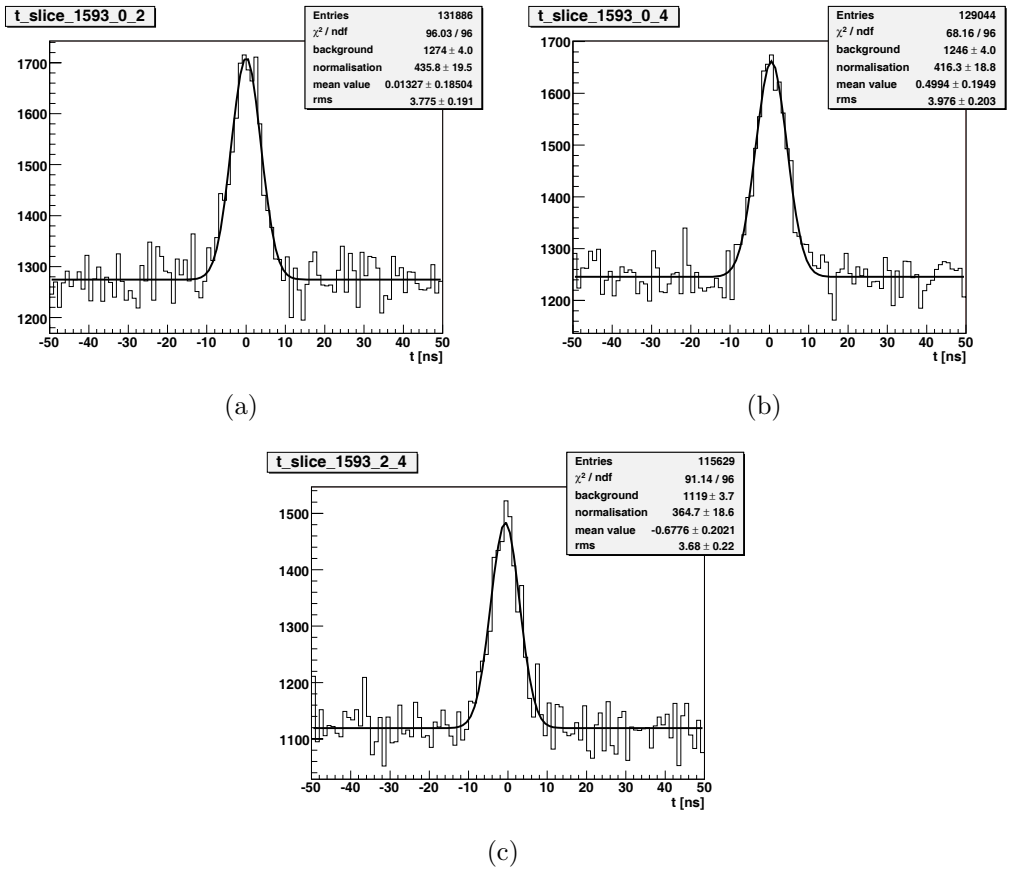

Figure 4.9: (a) Coincidence plot for the pair PMT 1 - PMT 2. (b) Coincidence plot for the pair PMT 1 - PMT 3. (c) Coincidence plot for the pair PMT 2 - PMT 3.

We have fitted each distribution using a combination of a gaussian and a flat background. After the fit, we compute the number of data combinations falling in a range centered around the maximum and having a width equal to $\pm 2\sigma$; we subtract the random background contribution and divide by the duration of the run. This yields the coincidence rate for each pair of PMTs;

the values are given in the table that follows. The errors are computed taking into account the number of events recorded and the error on the flat background parameter; other contributions are negligible.

PMT pair	Coincidence Rate (Hz)
1-2	13.00 ± 0.54 Hz
1-3	13.02 ± 0.55 Hz
2-3	10.55 ± 0.41 Hz

Fig.(4.10) shows the rates in the second half of 2005, separately for each combination of PMT pairs. In the long data empty period no runs taken with our analysis setup were available.

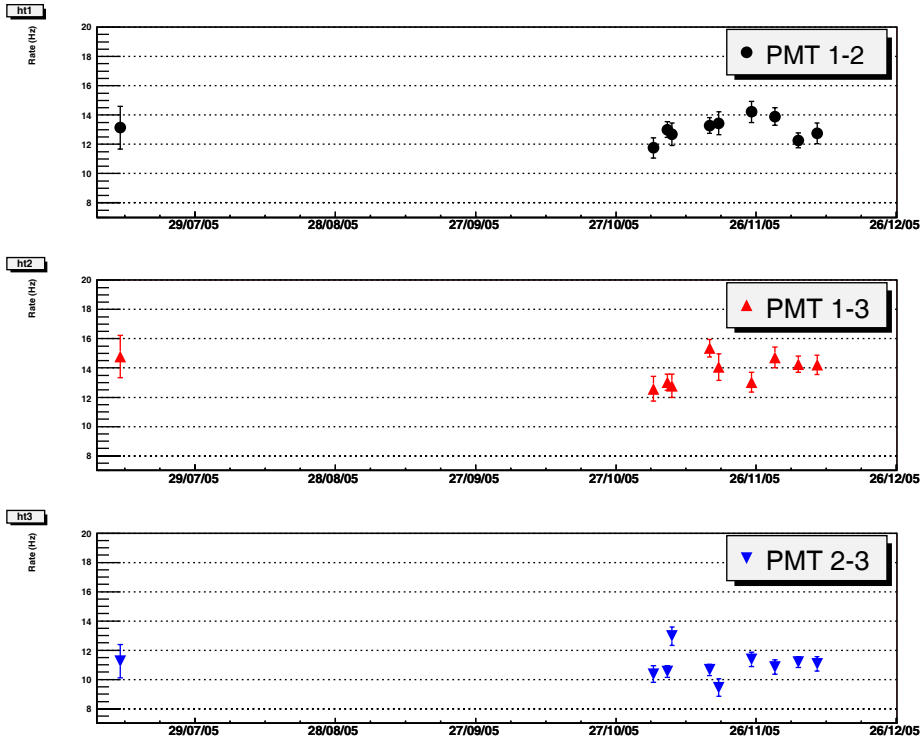

Figure 4.10: Coincidence rate registered by the three possible combination of PMTs of the MILOM middle storey, between July and December 2005.

We notice that combinations involving PMT1 have higher rates; however the coincidence rate per PMT is roughly constant over the whole period considered. This result allows us to interpret the coincidence events as ^{40}K signals, independent from time-varying bioluminescence activity.
In fact biological activity is known to produce light in an incoherent way [15]; this means that photons arrive uncorrelated on time scales of few nanoseconds. However radioactive decays may produce many photons within 1 nanosecond, giving raise to higher amplitudes on a single photomultiplier or tight coincidences on neighbouring photomultipliers.

The coincidence hits on two PMTs can also be used to check a posteriori the intercalibration in time of the ARS chips.
In fact, we expect the maximum of the Gaussian to be centered on zero, otherwise what we call coincidence events actually would not happen (statistically) at the same time. We can then run our analysis of the coincidence events over the twelve possible pairs of ARSs of the MILOM middle storey. Some examples are in fig.(4.11).
This effect could e.g. be due to slightly different ARS thresholds of the three PMTs. What we measure is usually consistent with 0; the largest value observed is 1.15 ± 0.17 ns.
The excellent angular resolution of the ANTARES telescope relies on the association of good timing information to the light signals recorded by the OMs. An accurate determination of a time offsets will contribute to improve the performance of the whole detector.

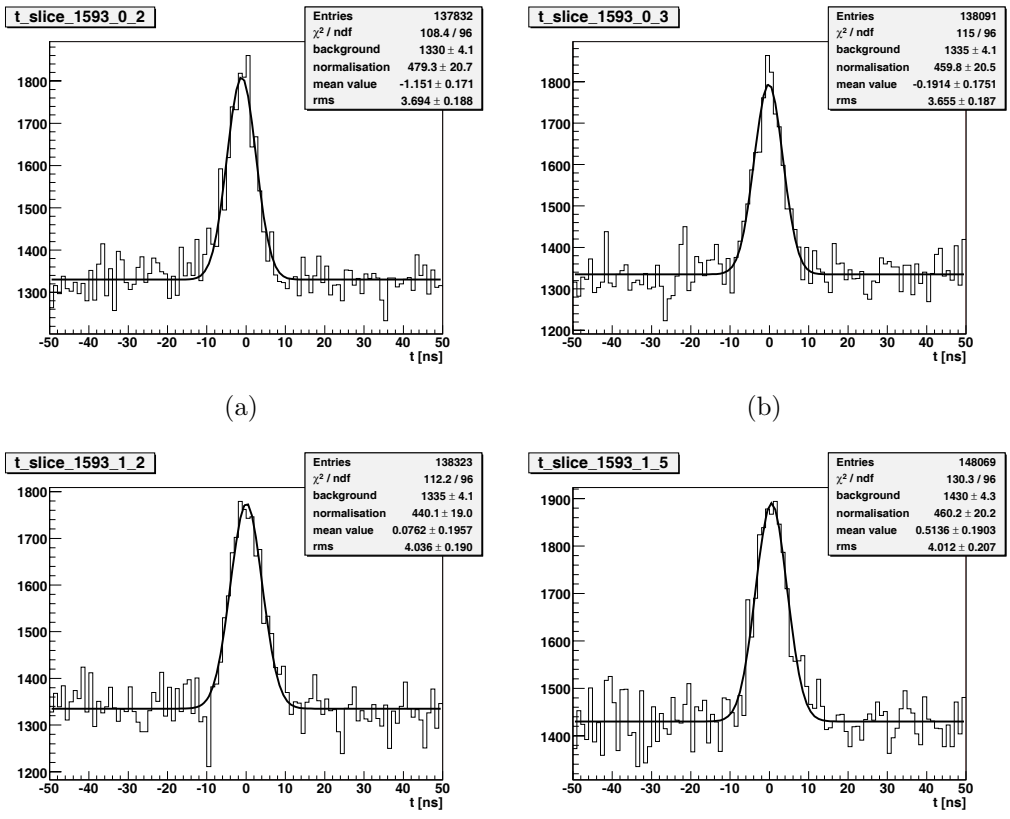

Figure 4.11: Coincidence plot for pair: (a) ARS 0 - ARS 2; (b) ARS 0 - ARS 3; (c) ARS 1 - ARS 2; (d) ARS 1 - ARS 5.

Chapter 5

The ANTARES trigger

The ANTARES trigger software [18] has to face the choice of sending all the data to shore: the digitised ARS data reach a flow of about 1 GB/s, which has to be filtered and reduced before writing to disk.

5.1 The trigger software

The design of the software is based on the object oriented approach and is written in C^{++} code. The input to the trigger process is given by the ARS raw data, i.e. time and charge information of the PMT hits, with an interface to the detector geometry and calibration values. The raw data are organized in so-called *TimeSlices*, which consist of frames with the data provided by ARSs in a time window of 13 ms.

The trigger program first performs a level 0 decoding (L0), represented by the simple conversion of raw data to calibrated data. After this step, the information of position, time and amplitude of the single hits are available. Level 1 decoding (L1) follows L0 and looks for coincidences, that is for pairs of hits recorded by two PMTs of the same storey, into a short time window (usually 20 ns wide).

After that, some different trigger algorithms have been developed, to investigate properly and efficiently different physics targets.

Trigger algorithms	
trigger1D	standard 1 dimensional trigger
trigger3D	standard 3 dimensional trigger
trigger3N	special 3 dimensional trigger
trigger3S	monopole trigger
triggerMX	mixed 1 dimensional trigger

The trigger1D implements the standard 1 dimensional trigger: taking into account the Cherenkov light propagation in water, it looks for time correlated hits from a candidate muon, whose track direction is given. The trigger3D, instead, does not fix any muon direction. The trigger3N acts like the standard 3 dimensional trigger, but in addition it makes for each trigger a scan of some given directions and applies the standard trigger1D for each direction. The trigger3S is conceived for slow moving particles ($\beta < 1$). The triggerMX is similar to the standard 1 dimensional trigger, but it requires a L1 as root hit, then it looks for time correlated hits along the assumed muon direction. The trigger logics above can operate on L0 as well on L1 input data; only triggerMX requires both L0 and L1. They also need some parameters to be specified: a minimum number of triggered hits (the so-called *minimum cluster size*); a time window into which hits can be considered time correlated; a *maximum transverse distance* (only for 1 dimensional triggers), which defines the maximum distance allowed between fired PMTs, on the plane perpendicular to the assumed direction. Suitable values are chosen, in order to increase the purity of the physics signal, with respect to the random optical background.
To avoid the duplication of output data, merging of events is used: after sorting the events in time, if the latest hit of an event is later than the earliest hit of the following one and if they have a hit in common, the events are merged.

The output of the different triggers contains a list of hits, which is used to build a *PhysicsEvent* object. The PhysicsEvents are stored on disk and can later be submitted to offline reconstruction algorithms, to perform the desired physics analysis.

5.2 Trigger performance

The performances of the different trigger approaches have been studied through MonteCarlo simulations in [18] and are here summarized. The main aspects to consider are the efficiency to detect a muon, the rate of accidental triggers due to random background and the number of CPUs needed to filter the data online.

The trigger efficiency to detect a muon is shown in fig.(5.1) as a function of the neutrino energy, for events which have at least six detected hits.

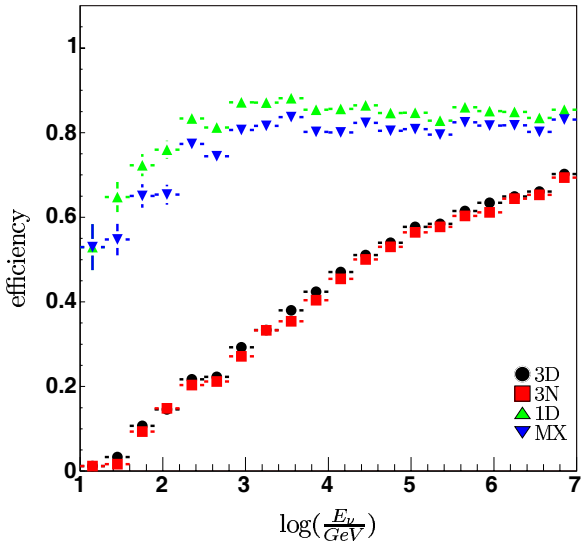

Figure 5.1: Trigger efficiency as a function of the neutrino energy.

The input to the 3 dimensional trigger algorithms (3D and 3N) corresponds to L1. The input to trigger1D corresponds to L0. TriggerMX takes both level 0 and level 1. The minimum cluster size has been set to 5 (6) for 3 (1) dimensional triggers. The direction used in the trigger1D and triggerMX is that of the MonteCarlo incident neutrino and the maximum transverse distance has been set to 90 m.

The trigger rate and the number of CPUs needed (evaluated for a 2.2 GHz frequency) are shown in fig.(5.2), as a function of the rate of single

background hits.

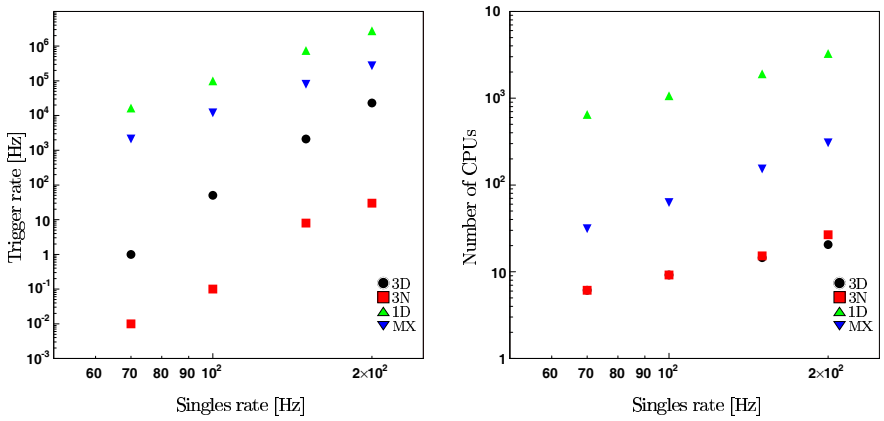

Figure 5.2: Trigger rate (left) and required number of CPUs (right) as a function of the rate of single background hits.

The trigger settings are the same as above, except for the direction used in 1 dimensional triggers, which has been set to horizontal. We notice that the efficiency of triggerMX is similar to that of trigger1D; nevertheless the required number of CPUs for triggerMX is reasonable.

The quality of the trigger is also related to the efficiency and the purity of the hit selection [fig.(5.3)], defined as

$$\text{efficiency} \equiv \frac{\sum_{trigger} \gamma_\mu}{\sum_{total} \gamma_\mu}, \qquad \text{purity} \equiv \frac{\sum_{trigger} \gamma_\mu}{\sum_{trigger} \gamma}.$$

The subscript *trigger* (*total*) refers to the triggered (all) hits in the event; μ refers to the photons that originated from the muon. The efficiency of 1 dimensional triggers is higher than that of 3 dimensional. The purity is about 90% (or more), when there are more than 15 photons from the muon detected.

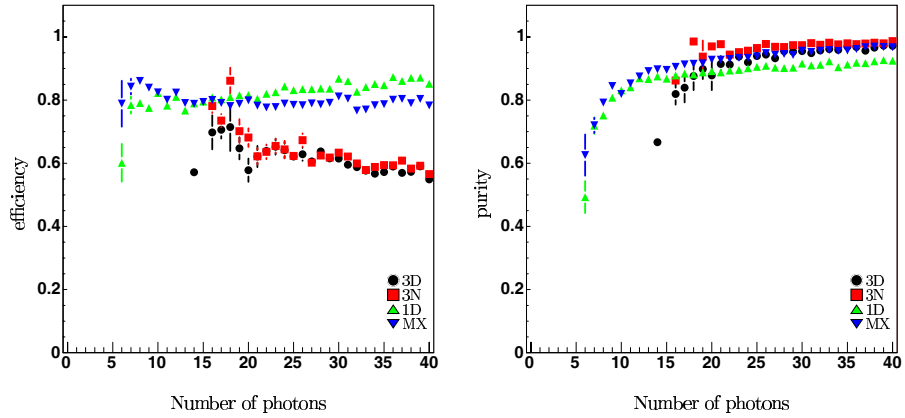

Figure 5.3: Efficiency (left) and purity (right) of the triggered hits as a function of the number of photons produced by the muon.

Chapter 6

Low energy track reconstruction with Prefit 1D

The research of neutrino point like sources is one of the main objectives of the ANTARES experiment. Therefore precise techniques for directional reconstruction are needed. Considering the energy regime accessible to ANTARES, since long a strategy for reconstruction of high energy neutrinos has been developed and improved [22]. For low energy neutrinos (E<10 TeV), a dedicated efficient strategy is still under development. Low energy reconstruction is complicated by the small number of hits generated on the PMTs. Moreover, the neutrino CC interaction produces a muon which is not aligned with the parent neutrino. For this reason it is necessary to consider properly the angular spread between the neutrino direction and the muon track. The *Prefit 1D* algorithm has been conceived for this purpose.

6.1 MC sample

The data analysed in this Chapter have been generated using the ANTARES MonteCarlo (MC) software. In particular, the packages used are *Genhen* 6.3 [19] for the neutrino generation and *KM3* 2.2 [20] plus *Geasim* 4.9 [21] for the propagation of tracks in water. The MC sample has been produced

requiring $5 \cdot 10^9$ neutrinos from a point source, distributed with a power law[1] $E^{-2.2}$ in the range (10 GeV-10 TeV). The chosen point source is the Galactic Centre (GC). The energy distribution of these neutrinos which produced muons at the detector is shown in fig.(6.1).

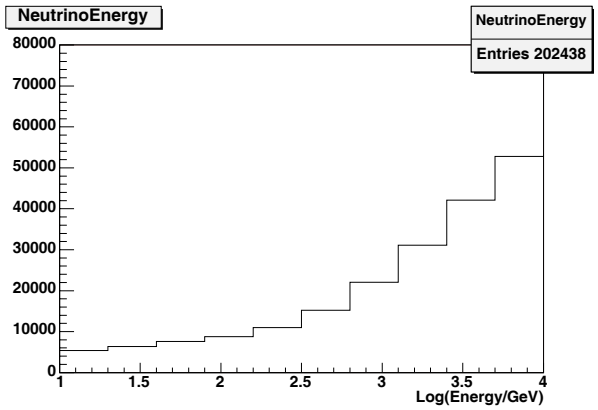

Figure 6.1: Energy distribution of MC neutrinos producing muons at the detector.

The hit digitization and the trigger logics have been simulated using the *TriggerEfficiency* program, included in the ANTARES-DAQ system. The output produced has been passed to the Prefit 1D analysis.

6.2 Prefit 1D

The Prefit 1D is an algorithm which processes triggered events and reconstructs tracks, assuming that we already know the neutrino direction. The attribute "1D" is derived from the search for hits aligned on a given direction.
Referring to the topology shown in fig.(6.2), the program defines a Cartesian reference frame, with the z-axis along the assumed neutrino direction. Then a fit of the track is performed using the fundamental equation

$$ct_i = ct_0 + (z_i - z_0) + \tan(\theta_c)\sqrt{(x_i - x_0)^2 + (y_i - y_0)^2}, \qquad (6.1)$$

[1] A power law $E^{-2.21}$ has been measured by Hess for Sgr A East (γ spectrum).

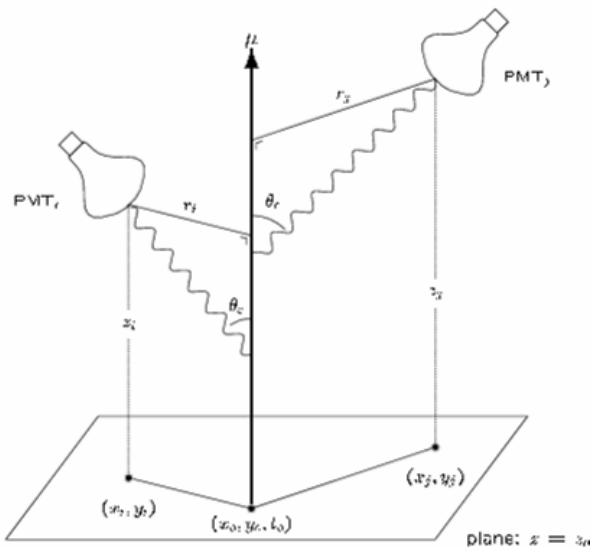

Figure 6.2: Frame for the reconstruction of the centre of gravity coordinates (x_0, y_0, z_0): z-axis along the ν direction.

where θ_c is the Cherenkov angle; the quantities labeled by i refer to the i-th triggered hit and represent the input to get those labeled by 0. (x_0, y_0, z_0) define the so-called *centre of gravity* of the event, that is the position where the muon is expected to pass at time t_0.
The fitting procedure is divided into four steps.

1. Charge weighted average prefit.
   The hit coordinates (x_i, y_i, z_i) are weighted with the amplitude a_i of the PMT signal:

$$x_0 = \frac{\sum_i a_i^2 x_i}{\sum_i a_i^2}, \quad y_0 = \frac{\sum_i a_i^2 y_i}{\sum_i a_i^2}, \quad z_0 = \frac{\sum_i a_i^2 z_i}{\sum_i a_i^2}.$$

   Then t_0 is computed as

$$t_0 = \langle\, t_i - \frac{(z_i - z_0) + \tan(\theta_c)\, r_i}{c} \,\rangle,$$

   defining $r_i \equiv \sqrt{(x_i - x_0)^2 + (y_i - y_0)^2}$.

2. Inverse transverse distance weighted average prefit.
   Taking z_0 and t_0 values found at step 1, we define $r'_i \equiv \frac{(t_i - t_0)\, c - (z_i - z_0)}{\tan(\theta_c)}$ and use it to weight x_0 and y_0 again:

$$x_0 = \frac{\sum_i \frac{x_i}{r'^2_i}}{\sum_i \frac{1}{r'^2_i}}, \qquad y_0 = \frac{\sum_i \frac{y_i}{r'^2_i}}{\sum_i \frac{1}{r'^2_i}}.$$

   A new t_0 is computed as in step 1.

3. Iterative scan using Simplex algorithm.
   The actual fit of the track is performed at this step, with a Simplex algorithm which takes (x_0, y_0, z_0, t_0) defined before as input parameters. An iterative procedure is performed to fit eq.(6.1). Improved values for x_0, y_0 and t_0 are defined at every iteration.

4. Least Square fit of t_0.
   Finally, a linear fit of t_0 is performed, taking into account the opening angle between the muon and the neutrino direction.

The χ^2 to be minimized at step 4 is

$$\chi^2 = (y - H\theta)^T V^{-1} (y - H\theta), \tag{6.2}$$

where

$$\Delta x_i \equiv x_i - x_0, \quad \Delta y_i \equiv y_i - y_0 \quad , \Delta z_i \equiv z_i - z_0,$$

$$y = \begin{pmatrix} t'_1 \\ t'_2 \\ \vdots \\ t'_n \end{pmatrix}, \quad t'_i = t_i - \frac{\Delta z_i}{c} - \frac{\sqrt{\Delta x_i^2 + \Delta y_i^2}}{c} \tan(\theta_c), \quad H = \begin{pmatrix} 1 \\ 1 \\ \vdots \\ 1 \end{pmatrix}, \quad \theta = (t_0).$$

The covariance matrix V contains the measurements uncertainties.

$$V = \begin{pmatrix} \sigma^2_{t,1} + \sigma_{\alpha,11} & \sigma_{\alpha,12} & \dots & \sigma_{\alpha,1n} \\ \sigma_{\alpha,21} & \sigma^2_{t,2} + \sigma_{\alpha,22} & \dots & \dots \\ \vdots & \vdots & \ddots & \vdots \\ \sigma_{\alpha,n1} & \dots & \dots & \sigma^2_{t,n} + \sigma_{\alpha,nn} \end{pmatrix}$$

$\sigma_{t,i}$ is the timing resolution (2.5 ns), while $\sigma_{\alpha,ij}$ accounts for the uncertainty in the muon direction:

$$\sigma_{\alpha,ij} = \frac{\partial t'_i}{\partial \alpha}\frac{\partial t'_j}{\partial \alpha}\delta\alpha^2.$$

The partial derivatives can be rewritten as

$$\frac{\partial t'_i}{\partial \alpha} = \frac{\partial t'_i}{\partial \Delta x_i}\frac{\partial \Delta x_i}{\partial \alpha} + \frac{\partial t'_i}{\partial \Delta y_i}\frac{\partial \Delta y_i}{\partial \alpha} + \frac{\partial t'_i}{\partial \Delta z_i}\frac{\partial \Delta z_i}{\partial \alpha}$$

and

$$\begin{aligned}
&\tfrac{\partial t'_i}{\partial \Delta x_i} = -\tfrac{\tan(\theta_c)}{c}\tfrac{\Delta x_i}{\sqrt{\Delta x_i^2+\Delta y_i^2}}, && \tfrac{\partial \Delta x_i}{\partial \alpha} = \Delta z_i\cos(\alpha) - \Delta x_i\sin(\alpha),\\
&\tfrac{\partial t'_i}{\partial \Delta y_i} = -\tfrac{\tan(\theta_c)}{c}\tfrac{\Delta y_i}{\sqrt{\Delta x_i^2+\Delta y_i^2}}, && \tfrac{\partial \Delta y_i}{\partial \alpha} = \Delta z_i\cos(\alpha) - \Delta y_i\sin(\alpha),\\
&\tfrac{\partial t'_i}{\partial \Delta z_i} = -\tfrac{1}{c}, && \tfrac{\partial \Delta z_i}{\partial \alpha} = -(\Delta x_i + \Delta y_i)\cos(\alpha) - \Delta z_i\sin(\alpha).
\end{aligned}$$

We can use the equations above to compute the t_0 value, which minimizes the χ^2, with

$$t_0 = \frac{\sum_i \sum_j V_{ij}^{-1} t'_j}{\sum_i \sum_j V_{ij}^{-1}}. \tag{6.3}$$

The performance of the centre of gravity reconstruction is verified triggering 100000 events from our generated MC sample and then applying the Prefit 1D algorithm. We chose triggerMX, specifying the direction of the Galactic Centre and asking for a cluster size of 6 hits, event merging and leaving the other settings with default values (see Chapter 5).
To define event by event the muon opening angle (the angle between the neutrino and the muon), we proceed as follows. The energy range considered (10 GeV-10 TeV) is divided in seven bins. Each bin is associated to the median of the distribution of the angular difference between the incident neutrino and the produced muon (ν_μ-nucleon interaction), in that energy interval. The relations are:

1. 10-20 GeV $\rightarrow 4.567°$,

2. 20-50 GeV → 3.419°,
3. 50-100 GeV → 2.447°,
4. 100-200 GeV → 1.909°,
5. 200-500 GeV → 1.294°,
6. 500 GeV - 1 TeV → 0.755°,
7. 1-10 TeV → 0.495°.

The MC information about the energy of the neutrino which generates the muon allows the choice of one of the angles above, as input to Prefit 1D.

The ANTARES reference frame (further called *detector frame*) is defined with the centre of the detector as origin and the z-axis oriented upward. For a single MC event, we can make in this frame an "event display": i.e. we show the position of the triggered hits, of the MC muon track and of the reconstructed centre of gravity in 2D projections [fig.(6.3)]. This single event clearly looks well reconstructed.
Moving to a frame (*muon frame*) with the interaction vertex as origin and the z-axis parallel to the muon direction taken from MC, the distributions[2] of the x and y coordinates of the reconstructed centre of gravity [fig.(6.4)] are centered near 0, with a rms less than 10 m.

The influence of the trigger model on the reconstruction must be checked as well. Therefore we analysed our MC sample both with the chain trigger3D-Prefit 1D and triggerMX-Prefit 1D. The trigger settings were L1 input[3], cluster size equal to 6, event merging and other with default values. We show

[2]The different shape between x and y distributions is due to the "quantization" of the detector in lines and storeys. It disappears for events with vertical direction (cylindrical symmetry [fig.(3.3)]).

[3]L1 input for trigger3D is the standard choice, because it has been shown that with L0 a big amount of optical background events pass the trigger condition.

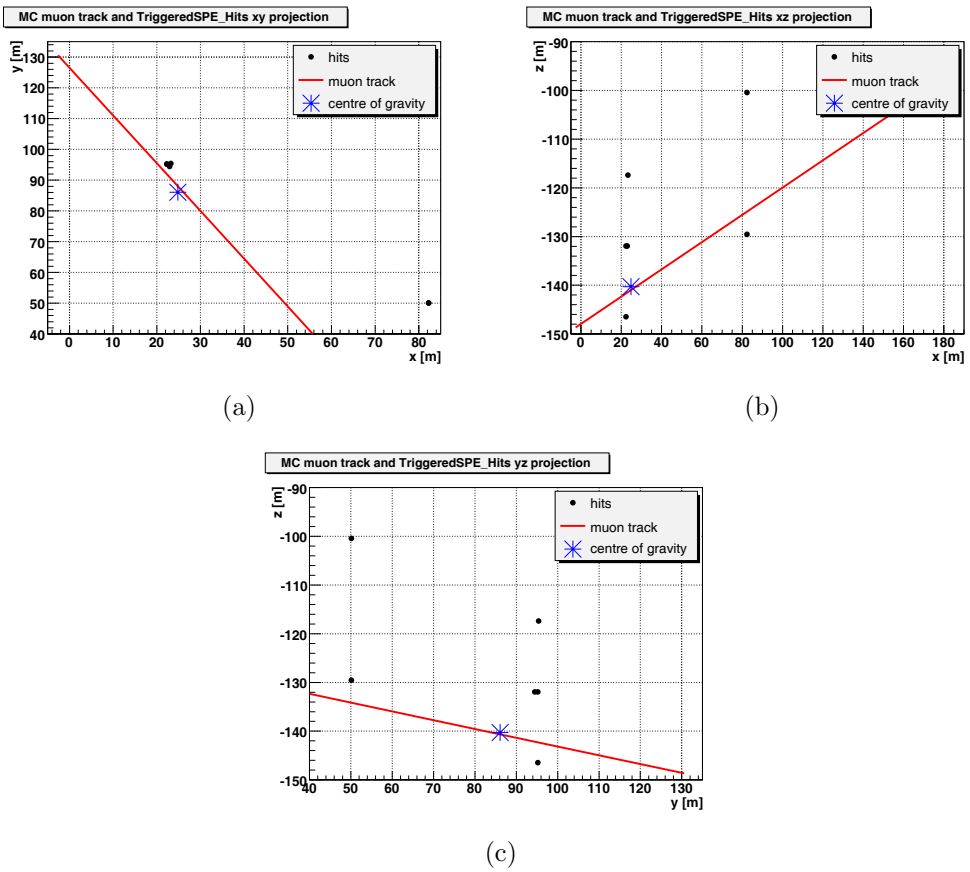

(a) (b)

(c)

Figure 6.3: Event display of a single MC event in projections of the detector frame: (a) xy; (b) xz; (c) yz.

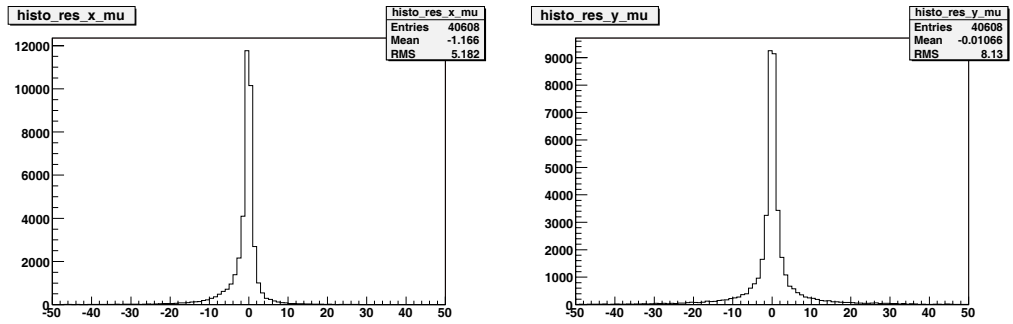

(a) (b)

Figure 6.4: (a) Distribution of the x coordinate of the reconstructed centre of gravity, in the muon frame. (b) Distribution of the y coordinate of the reconstructed centre of gravity, in the muon frame.

the 2D distance $\sqrt{x_0^2 + y_0^2}$ between the reconstructed centre of gravity and the MC muon track in the muon frame [fig.(6.5)]. In the case of the Prefit 1D algorithm used after triggerMX, the mean distance appears slightly smaller, but the number of reconstructed events is more than three times higher.
Therefore, from now on, for our reconstruction we will use only events triggered with MX logic (see Chapter 5).

6.3 Study of a neutrino spectrum from point source

The Prefit 1D may be applied in the study of a neutrino signal, generated by a point source according to an unknown energy spectrum. This signal is expected to be well simulated by the MC sample that we used so far: $5 \cdot 10^9$ neutrinos from the Galactic Centre (GC), producing 202438 muons to be triggered and reconstructed at the detector.

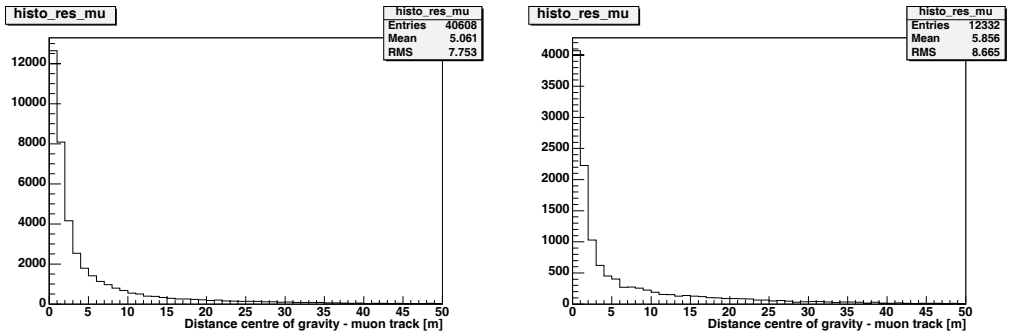

(a) (b)

Figure 6.5: Distribution of the distance between the centre of gravity and the MC muon track: (a) triggerMX events; (b) trigger3D events .

6.3.1 Angle selection

Given our interest in the low energy regime, when using data, the angle between the neutrino and the muon direction is not known, but has to be estimated for step 4 of Prefit 1D. Therefore, we perform a χ^2 minimisation for every angle value matched to the energy bins established above. A probability value (P_value), given by the cumulative χ^2 distribution, is calculated for the seven minima obtained.
To give a first estimate of the angle between the neutrino and the muon, we take the one associated with the biggest P_value; in addition we demand P_value< 0.95.

In fig.(6.6) we show a plot of the MC generated angle vs the reconstructed angle. The latter is badly shifted to big values. To avoid this behaviour, we apply a window of 0.1 width, into which we want to select our P_value: if, for instance, the smallest P_value obtained is 0.34, we take the biggest P_value smaller than 0.44. In this way, we avoid small angles being reconstructed as big, overestimating errors. We also demand P_value> 0.02 (badly reconstructed events accumulate near 0) and P_value< 0.95.

Then we try to constrain the angle selection further, using phenomenological information driven by MC. Since a mere energy estimator is not given,

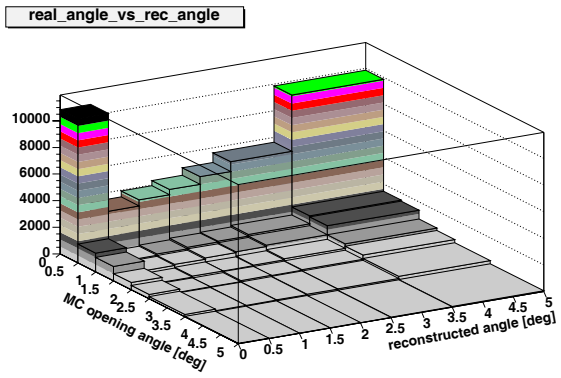

Figure 6.6: First reconstruction of the opening angle (see text).

we use the number of triggered hits per event instead: the more energetic a muon crossing the detector is, the bigger the amount of light produced. However, we must consider that if a very energetic neutrino generates a muon in the rock far under the instrumented volume, the muon looses a lot of energy before reaching the detector and the Cherenkov light produced may be very faint.

In fig.(6.7(a)) we show a scatter plot of the MC opening angle vs the number of triggered hits and in fig.(6.7(b)) a profile plot of that distribution. Referring to fig.(6.7(b)), we define the following cuts on the reconstructed events (θ_{sel} = angle selected through the P_value choice; n_{hits} = number of triggered hits).

θ_{sel}	<0.5	$0.5 \div 1.0$	$1.0 \div 1.5$	$1.5 \div 2.0$	$2.0 \div 2.5$	$2.5 \div 3.5$	>3.5
n_{hits}	> 7	$9 \div 29$	$9 \div 26$	$8 \div 22$	$8 \div 18$	$8 \div 15$	<13

With these cuts, we show in fig.(6.8) a new plot with the MC angle vs the reconstructed one. The angle reconstruction is clearly improved in comparison with fig.(6.6).

The quality of the choices made so far in the analysis of a neutrino spectrum from a point source is demonstrated by the small increase of the 2D mean distance between the centre of gravity and the muon track (muon frame): from 5.06 m to 5.35 m.

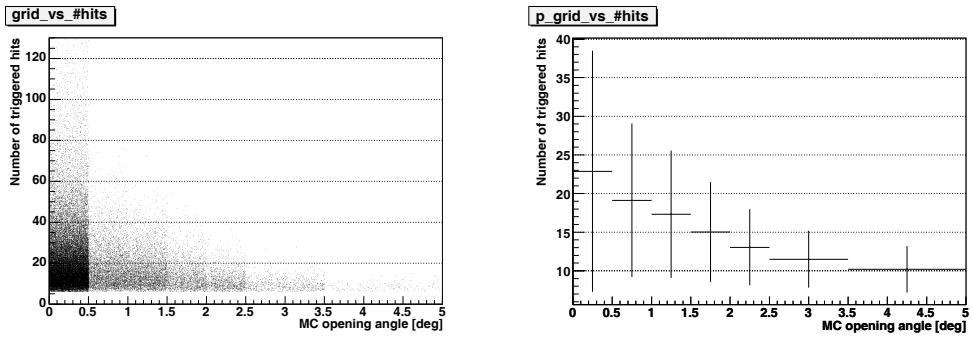

(a) (b)

Figure 6.7: (a) Scatter plot of the MC opening angle vs the number of triggered hits. (b) Profile plot of fig.(6.7(a)).

6.3.2 Study of random background

A fundamental aspect to consider in our study of the neutrino signal from point sources is the purity of the reconstructed signal, with respect to the random optical background.
Therefore we used a program (*RandomTimeSliceWriter* in the ANTARES-DAQ system) to generate 1000 timeslices - which correspond to 13 s of data taking - containing purely 70 kHz random background. Then we ran triggerMX, assuming a vertical neutrino direction. This choice represents "the worst case" for background analysis, since the detector is more efficient in revealing vertical events. The rate of triggered events is 1.1 kHz, but after filtering with the Prefit 1D algorithm and using our selection technique, it is reduced to 37.6 Hz. Unfortunately, the rate of reconstruction of these pure background events is still too high. Therefore, some experimental cuts have been defined considering the complete randomness of hits in these events: we expect that these hits have a larger average distance from the reconstructed centre of gravity than the physical signal [fig.(6.9)]. Thus we decided to apply the following constraints:

- maximum transverse distance = 76 m (defined in Chapter 5 as the maximum distance allowed between two hits, projected on a plane per-

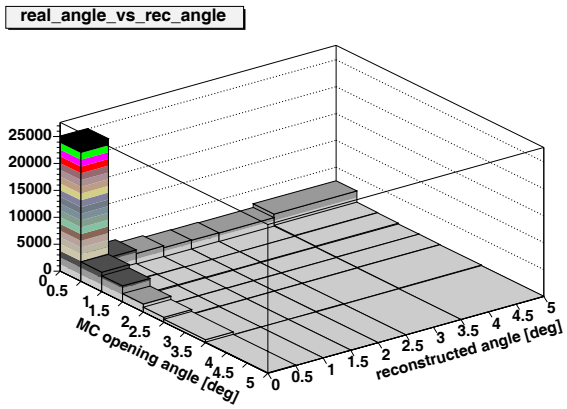

Figure 6.8: Second reconstruction of the opening angle (see text).

pendicular to the assumed neutrino direction; the default value is 90 m);

- only one triggered hit per events allowed further than 55 m from the centre of gravity (distance computed with hits projected on the plane containing the centre of gravity and perpendicular to the assumed neutrino direction).

These cuts reduced the random background reconstruction rate to 0 Hz.

Assuming time intervals between reconstructed background events exponentially distributed, the probability to see a signal is

$$\int_0^{13\mathrm{s}} \frac{1}{\tau} e^{-t/\tau} dt,$$

where τ has to be estimated from data. The number of events detected in 13 s is Poisson distributed $P(r|\mu) = \frac{e^{-\mu}\mu^r}{r!}$. Given $r = 0$, we choose a confidence level $\alpha = 95\%$ and we can estimate τ as follows:

$$P(r = 0|\mu) = e^{-\mu} = 1 - \alpha, \quad \mu = -\frac{1}{ln(1-\alpha)} = 0.334;$$

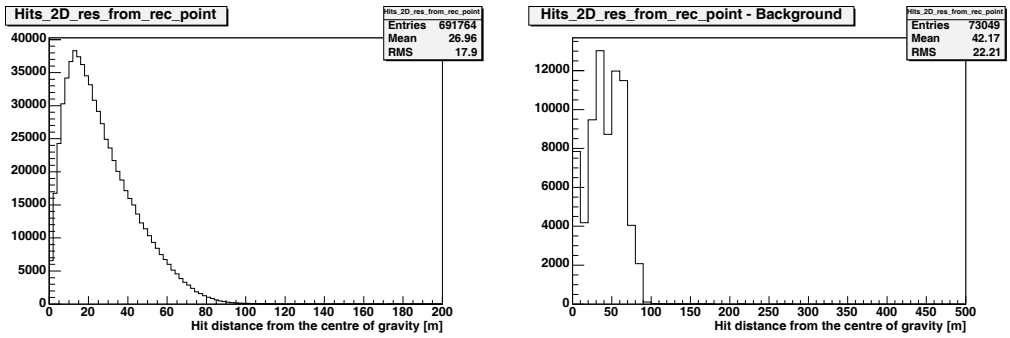

(a) (b)

Figure 6.9: Distribution of the distance between the triggered hits and the centre of gravity for: (a) MC sample; (b) reconstructed background.

$$N_{trigg} = 14375 \rightarrow \text{number of triggered background events in 13 s;}$$

$$N_{exp} = 13 \cdot \frac{N_{trigg}}{\tau} \equiv \mu \rightarrow \text{number of events expected in 13 s;}$$

$$\tau = 13 \cdot \frac{N_{trigg}}{\mu} = 5.6 \cdot 10^5 \text{ s} \sim 155 \text{ h.}$$

I.e. we expect to reconstruct one triggered background event per ∼155 hours. We recall that this is estimated for a 70 kHz continuous background. Considering the variations in time of the background rate observed in MILOM data (see Chapter 4), when analysing detector data in future, it will be necessary to repeat the simulation with the measured rate and verify again the power of background rejection.

We also take into account the effect of background hits, which happen to be causally (space-time) related to pure signal hits and then triggered. For that, we used the program *SummaryTimeSliceWriter* [24] in the ANTARES-DAQ system and a MILOM file recorded in October 2005 - in which the information about the measured optical background is collected - to add random hits to our original pure MC sample.

The performance of the whole reconstruction strategy (random background events rejection included) is shown in the next section.

6.3.3 Performance of the reconstruction

From our sample of 202438 MC muons giving detactable light and after adding the background measured by MILOM, we trigger 92751 events. The angle reconstruction in the Prefit 1D is succesful for 22951 events; after using the cuts for random background rejection, 10325 events remain.

It is possible to interpret the angle selection as an energy reconstruction: the seven angles are directly related to seven energy ranges (see section 6.2). Using the MC information, we show (in percentages) the relations between the neutrino energy and its reconstructed value.

	$\mathbf{E}_{rec}$ **(GeV)**						
$\mathbf{E}_{real}$ **(GeV)**	10-20	20-50	50-100	100-200	200-500	500-10^3	10^3-10^4
10-20	0.23	0.09	0.20	0.06	0.09	0.0	0.34
20-50	0.22	0.07	0.10	0.08	0.09	0.09	0.34
50-100	0.11	0.09	0.11	0.11	0.08	0.11	0.39
100-200	0.11	0.07	0.08	0.08	0.12	0.11	0.43
200-500	0.07	0.05	0.07	0.11	0.11	0.13	0.46
500-10^3	0.07	0.05	0.07	0.10	0.10	0.14	0.47
10^3-10^4	0.07	0.05	0.06	0.08	0.10	0.14	0.50

To increase the efficiency of signal detection, we can recover the events not passing the angle selection, by setting for them an arbitrary opening angle equal to 0, and re-run the Prefit 1D. When using this recovering option, we will refer to such a reconstruction as a technique with *unknown opening angle allowed*. With this option applied, the whole number of reconstructed events reaches 19496.

These values can be easily summarized in effective volume and effective area plots (see Chapter 3) [figs.(6.10)-(6.11)], in which trigger and Prefit 1D curves are shown as a function of the neutrino energy. We notice the loss of signal between the trigger and the reconstruction steps. Moreover, when we use the technique with an unknown angle allowed, the efficiency of the standard reconstruction is improved.

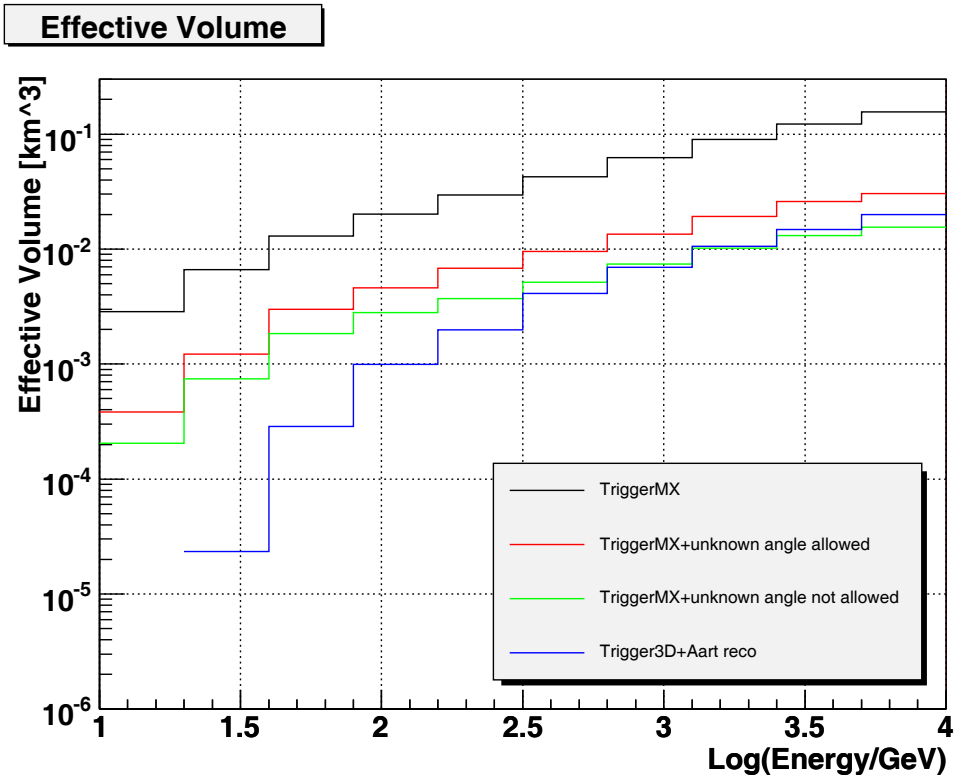

Figure 6.10: Effective volume of the detector after trigger and several different reconstruction methods.

In the same plots, we show the performance of the analysis chain trigger3D plus ANTARES standard event reconstruction (improved by Aart Heijboer [22]), using our MC sample. This reconstruction technique is used to observe the whole sky and search for point sources, trying to define their position. To make a comparison with our results, we have accepted all so-

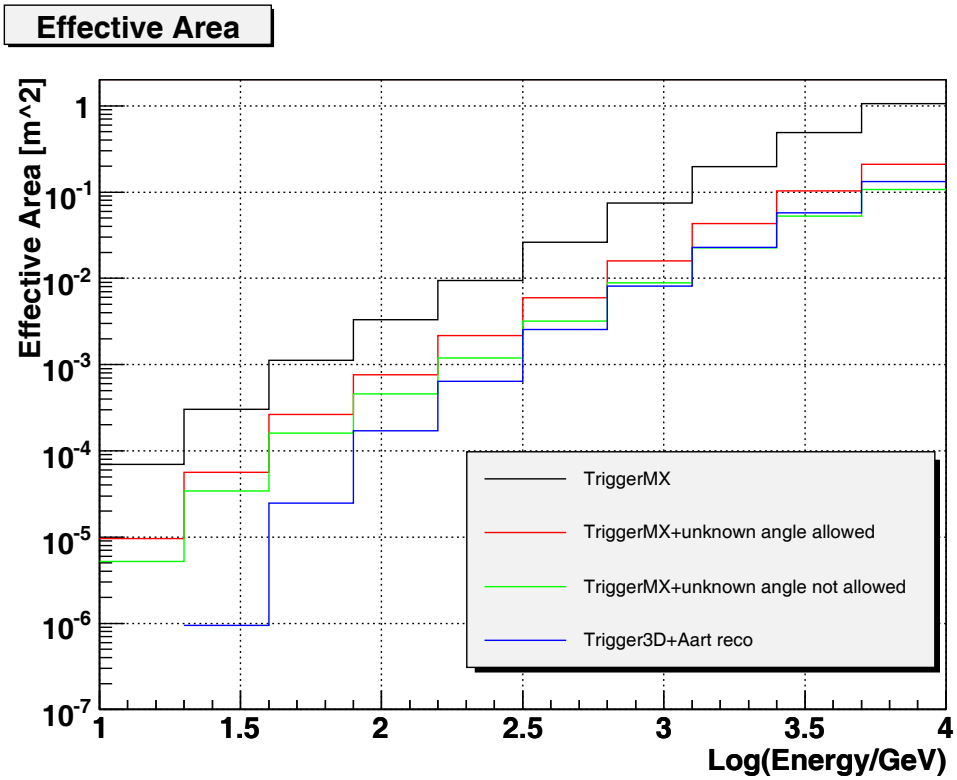

Figure 6.11: Effective area of the detector after trigger and several different reconstruction methods.

called Aart reconstructed events from our MC sample, which give the point source position not further than 4.57° from the GC. This is the maximum opening angle between ν_μ and μ that we take into account; it is matched to the energy bin 10-20 GeV, where the number of MC events is very low [fig.(6.1)]. Therefore we consider 4.57° a conservative value.
In fig.(6.12) we show the increase in effective volume achieved by Prefit 1D with respect to the standard reconstruction: the blue bars give the percentage of Prefit 1D signal (with unknown opening angle allowed) which Aart technique is able to reconstruct, per energy bin.
From the plot we conclude that the Prefit 1D is better than the standard reconstruction strategy over the whole considered energy range.

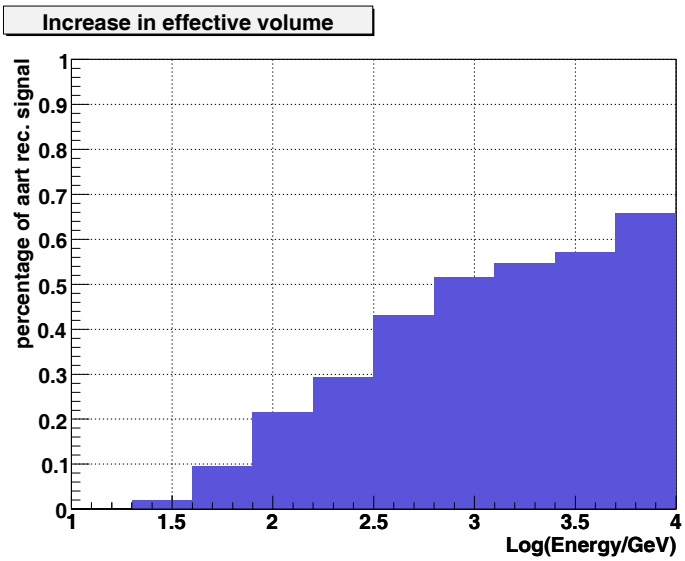

Figure 6.12: Percentage of Prefit 1D signal (with unknown opening angle allowed) which Aart technique is able to reconstruct, per energy bin.

6.3.4 Atmospheric neutrinos reconstruction

A source of physical signal which may be reconstructed by Prefit 1D is represented by atmospheric neutrinos. They are copiously produced by cosmic rays in Earth atmosphere, just in the energy range of our interest.
This kind of signal has been extensively studied by the ANTARES collaboration, for the purpose of separating neutrinos produced in the atmosphere from extraterrestrial ones.

We used a MC sample of 10 GeV-10 TeV atmospheric neutrinos, generated according to the Bartol flux model [23] and available for the collaboration ('Muon neutrinos 2004'), to check how many of these events will be reconstructed by the chain triggerMX-Prefit 1D, specifying a vertical neutrino direction (this will be the choice made from now on, for every atmospheric or random signal analysis). The equivalent time of the generation is ∼14000 s. Using the MC information of detected neutrinos, it is possible to estimate the number of expected events per year [25]. In fig.(6.13) we show the con-

tributions to this number from atmospheric neutrinos into the seven energy bins used for angle selection.
The expected number of events per year is 1404 ± 126 with unknown opening angle allowed, otherwise it reduces to 1023 ± 105 [26].

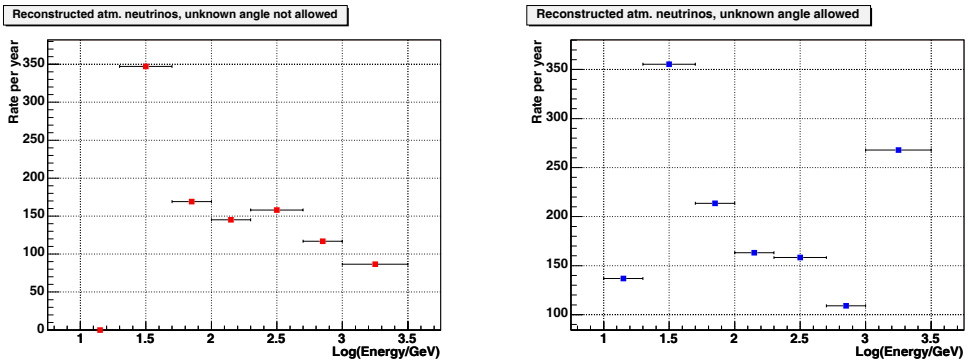

(a) (b)

Figure 6.13: (a) Expected number of atmospheric neutrino events per year, in the seven energy bins used for angle selection. (b) Same as fig.(6.13(a)), with unknown opening angle allowed.

We notice that the largest contribution comes from neutrinos with low energy (20-50 GeV). If we use the technique with unknown opening angle allowed, the number of events in the most energetic bin increases a lot, since these events are easiest recovered when setting the opening angle equal to zero.

6.3.5 Atmospheric muons reconstruction

Muons produced in the atmosphere by cosmic rays may represent another source of undesired physical signal in our search for neutrino point sources. However, their detection rate is expected to be negligible compared to that of atmospheric neutrinos, because - given the Earth shield - only downward going muons reach the detector and the reconstruction technique is optimized for upward going neutrino-induced muons.

As for the atmospheric neutrinos, we analysed a MC sample of atmospheric muons available for the collaboration ('Corsika 2003 km3 level') [27], generated by proton primary particles in the energy range 1 TeV-10^5 TeV and in the two zenith angle ranges $0^\circ - 60^\circ$, $60^\circ - 85^\circ$. With lower primary energies, no muons able to reach the detector are produced. The analysis results are in the next table.

Energy (TeV)	1-10	10-100	10^5	1-10	10-100	10^5
Zenith (deg)	0-60	0-60	0-60	60-85	60-85	60-85
Gen. time	∼3 min	∼2.4 h	∼6 days	∼1.8 min	∼3 h	∼6 days
MC events	10103	296153	$2.28 \cdot 10^6$	53	33318	514690
Triggered	482	64132	391834	4	2294	68678
Reconstructed	0	0	0	0	0	0

6.3.6 Separation of close sources

It is important to verify how well our reconstruction works in the case of two point sources separated by a few degrees in angular distance. For this we used our sample of MC events from GC and we ran triggerMX plus Prefit 1D, with a direction increased by a few degrees in zenith angle (detector frame). In fig.(6.14) we show the percentage of reconstructed events with respect to the events selected pointing to the GC. From the plot we can read, for instance, that given the GC and a source radiating the same flux at a position 8° away from it, the signal of the GC is 70% increased by neutrinos coming from the other source (unknown opening angle allowed).

6.3.7 Summary of spectrum analysis

The feasibility of studying a neutrino spectrum from a point source with Prefit 1D has been demonstrated; in particular, the reconstruction of the centre of gravity of the event performs well.
Assuming the predictions of Bartol model and consequently the expected atmospheric neutrino events per year, assuming also that the neutrino reconstruction follows a Poisson distribution, the number of detected events

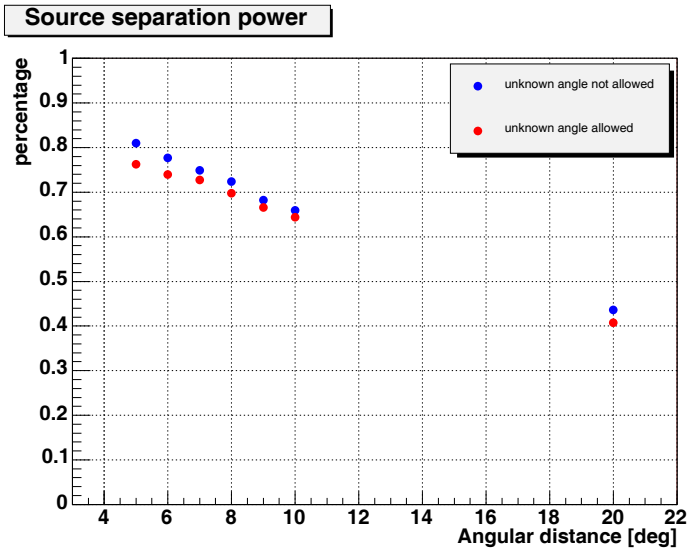

Figure 6.14: Percentage of reconstructed events (with respect to events selected pointing to the GC), when the assumed neutrino direction is shifted by a given angular distance in zenith angle (detector frame).

per year required to identify a point source at 5σ is 1591 - with unknown opening angle allowed - or 1183. This value is strongly model dependent and relies on MC settings and generation time. With a working detector, it would be useful to compare the reconstructed signal from a candidate point source direction, with some other random direction observations.

The large estimated number of atmospheric neutrinos seen and the source separation power of Prefit 1D reconstruction suggest that many "weak" sources may not be distinguished from other signals on a long observation campaign. However, this low energy spectrum analysis is considered to fit well the detection of strong point sources or transient phenomena producing neutrinos - such as supernova explosions and GRBs.

6.4 Reconstruction of neutrinos with defined energy

The next step of our study has been devoted to the reconstruction of a neutrino signal from a point source, with an estimated energy within one of the seven energy bins defined in the previous section for angle selection. This analysis is thought to establish a good detection power for neutrinos produced by expected physics processes, such as SUSY DM annihilation.
For this purpose, we can use our MC sample, keeping in mind that the -2.2 spectral index of generation is not related to any physics assumptions and all the energy bins are taken into account separately.

The reconstruction of neutrinos with defined energy is accomplished with the same experimental cuts on the number of triggered hits (per opening angle value) and hit distances, explained in the spectrum analysis section (section 6.3): these cuts are optimized to maximize the interesting signal purity, against random background and atmospheric neutrinos events. The only difference with respect to the previous analysis relies on the direct choice of the opening angle for every event, using MC energy information; again a (0.02<P_value<0.95) allowed range is used.
Unfortunately, according to the analysis of our 13 s sample of pure triggered background, it is not possible to completely avoid the random background reconstruction: for the 10^3-10^4 energy bin we record only one event, which corresponds to a rate of $7.692 \cdot 10^{-2}$ Hz. For the other bins we still expect to reconstruct one background event per $\sim$155 hours (see previous section).

With regard to the atmospheric neutrino background signal, the situation for the spectrum analysis is now much improved. Using the MC atmospheric neutrino sample of the previous section, with the demand for a precise opening angle we strongly reduce the reconstruction of undesired events around the given source direction.

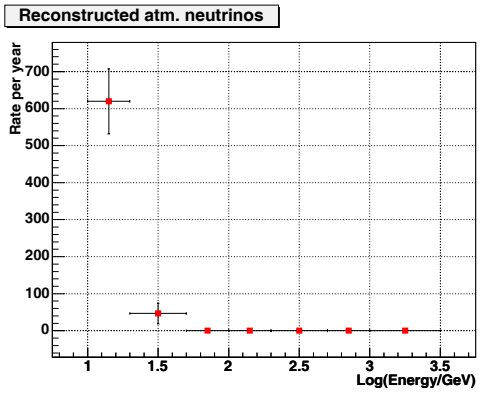

Figure 6.15: Expected atmospheric neutrino events per year per energy bin (neutrinos with defined energy).

The number of expected events per year per energy bin is shown in fig.(6.15) and specified in the following table, with the number of events needed to claim a point source discovery at 5σ level.

Energy range (GeV)	**Expected events per year**	**5σ events**
10-20	620 ± 9	744
20-50	46.6 ± 5.3	80.7

No atmospheric muons are reconstructed for all the energy bins considered.

6.4.1 Performance of the reconstruction

The quality of event reconstruction obtained with Prefit 1D for neutrinos with defined energy is demonstrated by the small mean value (only 5.68 m!) of the distance between the reconstructed centre of gravity and the MC muon track [fig.(6.16)].

It appears that given a model predicting a neutrino flux within one of our energy bins, it is possible to use the effective volume or effective area values - plotted in figs.(6.17)-(6.18) - to directly estimate a neutrino interaction rate (see section 3.3.1).

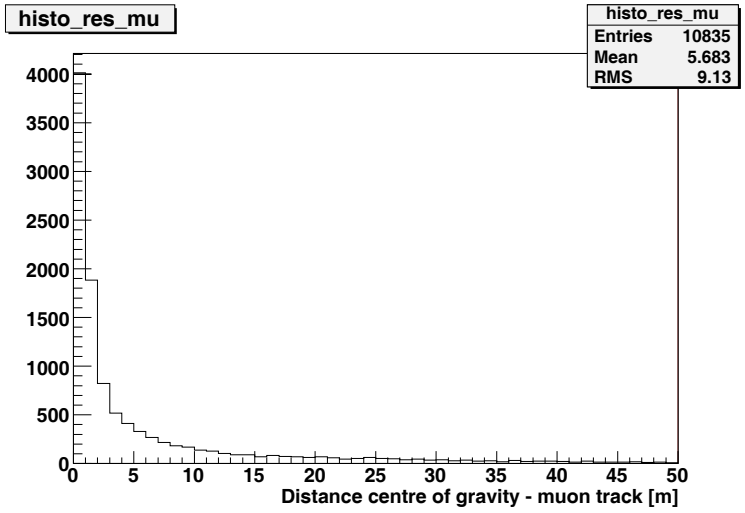

Figure 6.16: Distribution of the distance between the centre of gravity and the MC muon track (neutrinos with defined energy).

In the same figures, we also show the effective volume and effective area for MC events giving muons at the detector and for triggered events. This allows to check the signal loss at every simulation step, up to the final event reconstruction.

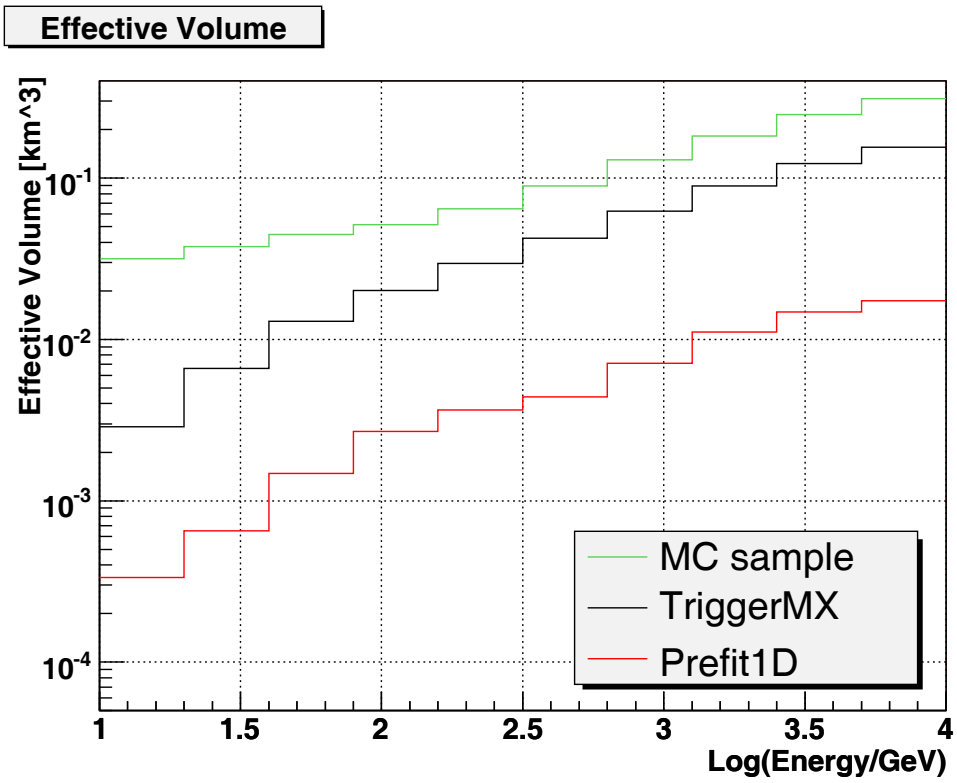

Figure 6.17: Effective volume of the detector for MC, triggered and reconstructed events (neutrinos with defined energy).

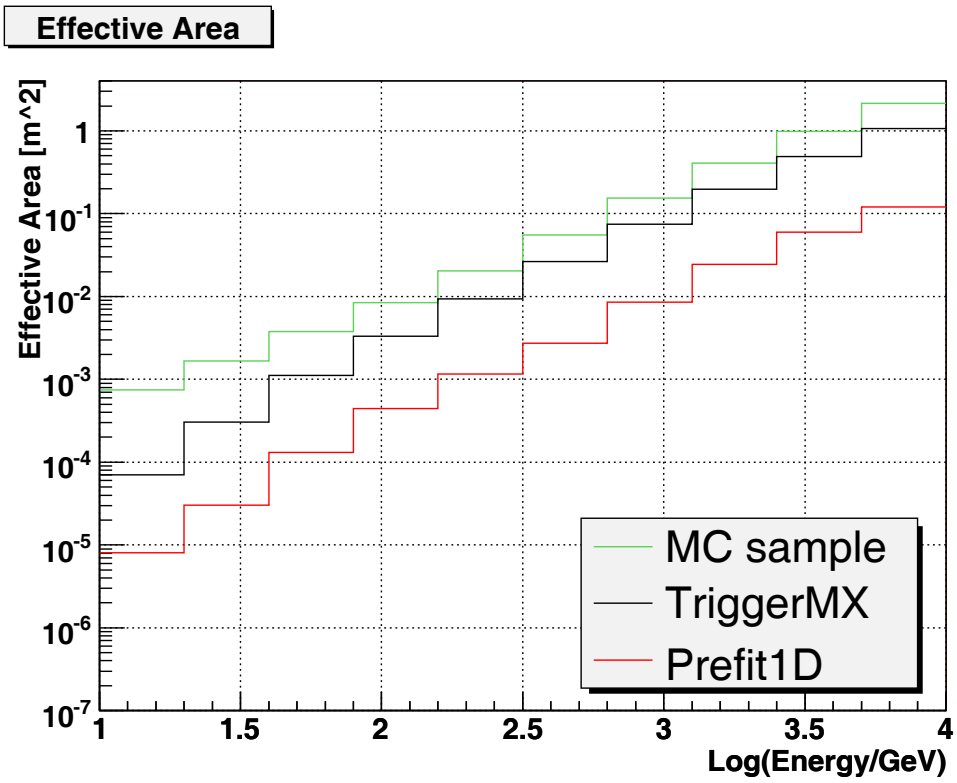

Figure 6.18: Effective area of the detector for MC, triggered and reconstructed events (neutrinos with defined energy).

Chapter 7

Analysis of LINE1 data

The first full detector line (LINE1) of ANTARES has been deployed at the experiment site in February 2006 and connected on March 2^{nd} 2006. Since this date, the data acquisition is operational. While this Chapter is being written (March 23^{rd} 2006), many muon tracks have already been reconstructed by Collaboration members.

7.1 LINE1 data acquisition

LINE1 is the first fully equipped string of ANTARES: it holds 25 storeys, with 75 OMs (150 ARSs). Since its connection, the electronics and data acquisition system have worked properly. The online trigger used so far is trigger3D, with L1 inputs.
Unfortunately the optical background rates measured since LINE1 operation are higher than what MILOM recorded by the end of 2005; the baseline reaches order of a few hundreds of kHz. However the trigger settings chosen are able to filter this high rate background and to provide candidate muons for track reconstruction.

7.2 Muon reconstruction

Since the position calibration of every storey of LINE1 is still in progress, the data analysis developed so far assumes that the line is perfectly vertical. This azimuthal symmetry has been considered in [28], where a muon track fitting procedure for LINE1 is defined through a scan over a set of zenith angle directions. The track parameters are estimated in a way similar to the Prefit 1D algorithm, after rotating the z-axis of the detector frame in every direction considered.
This gives a collection of candidate tracks, which provide the starting values for an iterative procedure to fit also the zenith angle and define accurately the track. The details of this technique are explained in [28]; the results obtained will soon be published by the Collaboration.

An example of a fitted muon track is presented in fig.(7.1), where the z-position of triggered hits are shown versus the recorded hit time. The straight line represents the fitted track.
The analysis of data taken during the first week of operation resulted in a few thousands reconstructed events and a preliminary zenith angle distribution dominated by downward going atmospheric muons. Also some candidate upward going tracks were reconstructed. Systematics are being studied.

7.3 Prefit 1D for LINE1 analysis

Following big excitement about the successful connection of LINE1, we had a first look to the data recorded. However we must be aware that the Prefit 1D algorithm has been conceived to work on triggerMX data and its performance has been studied for the complete ANTARES detector and with late 2005 background conditions. In particular, the steps of the algorithm analysing distances between hits require at least two strings to work as desired.
Therefore, the reconstruction of the centre of gravity is much less precise when using hits belonging to only one line: the analysis of the MC sample of Chapter 6 shows a mean distance between the reconstructed point and the MC muon track of about 16 m (it was about 5 m with the full detector).

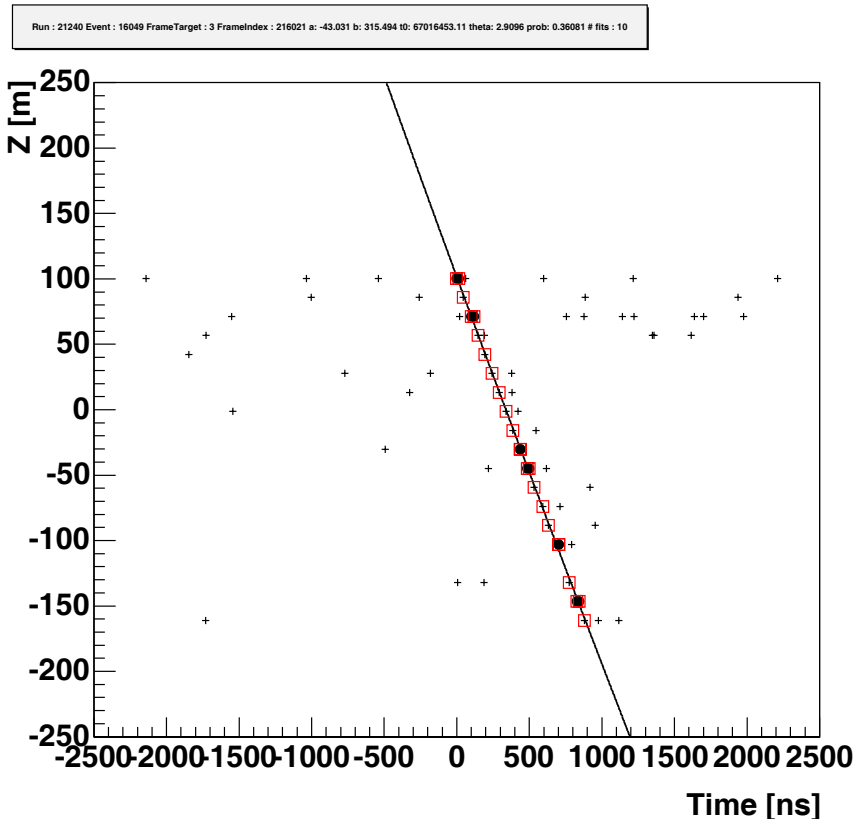

Figure 7.1: Event display taken from [28]. Taking a vertical z-axis, the black dots represent the L1 triggered hits, the crosses show the L0 hits in coincidence with the event and the red squares specify the hits used in the fit. The straight line represents the fitted muon track.

The effective volume is about a factor 9 smaller than what we found for a 12 strings setup.

Keeping in mind the remarks above, we decided to modify our analysis program to read LINE1 data, to calibrate the triggered hits with an interface to the database with ARSs calibration information and to eventually reconstruct upgoing muon tracks, assuming a vertical direction.
The next table summarizes the results obtained.

Run	date	duration	triggered	rec. 1	rec. 2	rec. 3
21218	03/03	6m 24s	2438	0	0	0
21219	03/03	2h 22m 33s	81	0	0	0
21220	03/03	11m 1s	62	0	0	0
21221	04/03	8h 25m 54s	146	0	0	0
21225	04/03	1h 26m 2s	660	0	0	0
21226	04/03	1h 13m 36s	556	0	0	0
21229	04/03	29m 36s	1640	0	0	0
21230	04/03	15m 16s	288	0	0	0
21231	04/03	1h 23m 53s	1545	0	0	0
21233	04/03	8h 25m 13s	29106	0	0	0
21234	05/03	8h 25m 13s	29433	0	0	0
21235	05/03	3h 50m 57s	13342	0	0	0
21240	05/03	8h 25m 9s	29481	0	0	0
21241	**06/03**	**6h 31m 48s**	**23286**	**0**	**1**	**0**
21242	06/03	49m 34s	1984	0	0	0
21257	07/03	2h 56m 57s	10403	0	0	0
21259	07/03	45m 9s	2338	0	0	0

with:

- rec. 1: reconstruction with angle selection;
- rec. 2: reconstruction with angle selection and unknown opening angle allowed;
- rec. 3: reconstruction of neutrinos with defined energy (one reconstruction trial for each of the seven energy bins).

One upward going vertical track is found in run 21241, applying the reconstruction technique used in Chapter 6 for the study of a neutrino spectrum. The event is displayed in fig.(7.2).

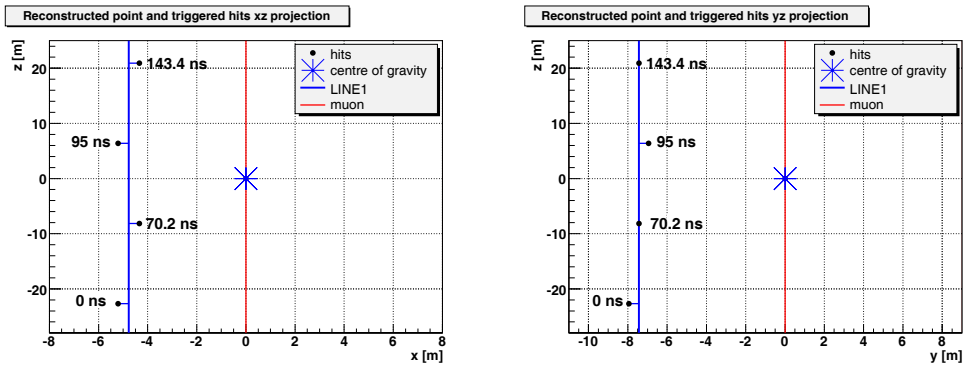

(a) (b)

Figure 7.2: (a) Display of the event reconstructed from run 21241: the position of the reconstructed centre of gravity and of the triggered hits are shown in a xz projection of the detector frame, whose origin has been moved over the reconstructed point. Time 0 is assigned to the hit which is the nearest to the sea bottom; the other hit times are computed from this starting point. (b) As in fig.(7.2(a)), with yz projection.

A check of the optical background condition for this run is clearly needed. We first looked at the number of hits recorded by the 150 ARSs of the line per timeslice. Fig.(7.3) shows the number of hits recorded by each ARS at the different floors, in a randomly chosen timeslice. We can read that a few thousands of hits (3000 hits = ∼57 kHz) are recorded at the first floors

(storeys near to the sea bottom); moving upwards the rates increase (20000 hits = ∼380 kHz) and the PMTs at the highest storeys are blinded by the background.

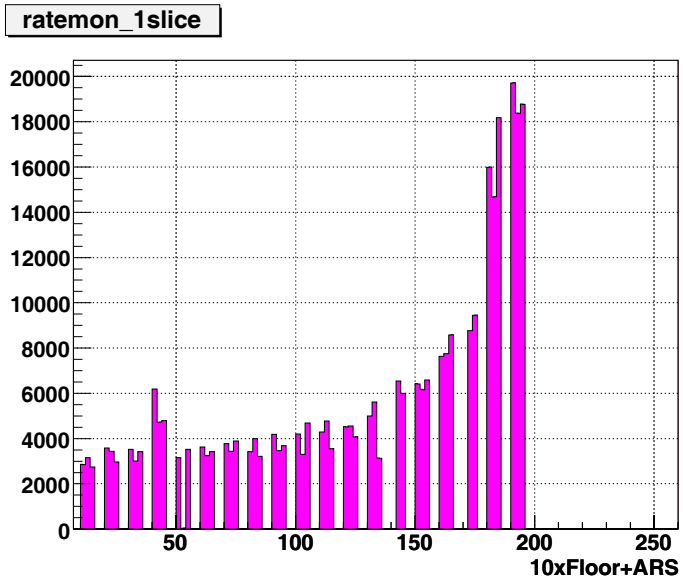

Figure 7.3: Histogram of the number of hits recorded in each ARS at the different floors, in a randomly chosen timeslice (run 21241). Floor 1 refers to the storey at the bottom of the line.

The results of the same analysis of the full run (223759 timeslices) are shown in fig.(7.4). There we see highest rates at storeys 10-14; then PMTs at the upper floors begin going to XOffs and record less hits.
A tool to simulate the dependency of the rate on depth and, in particular, to take into account the blinded floors has been introduced in the ANTARES-DAQ system. Therefore we generated 100000 timeslices filled with just the background recorded during run 21241; then we applied the trigger settings of LINE1, followed by our Prefit 1D. No pure background events were reconstructed.

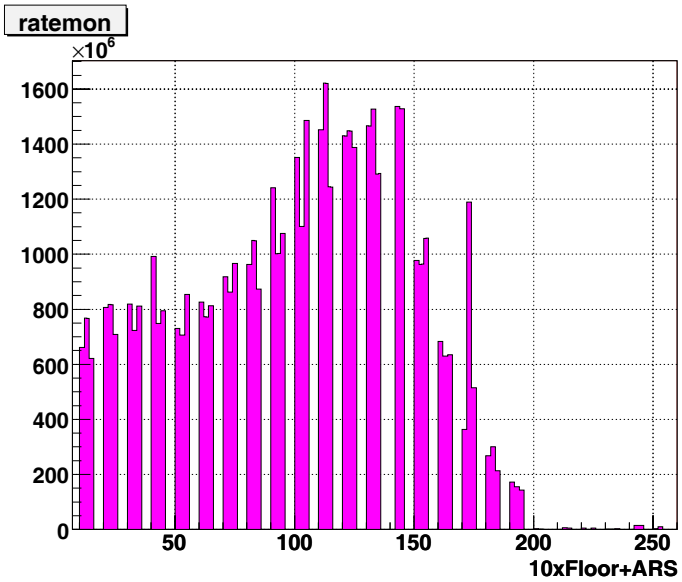

Figure 7.4: Histogram of the number of hits recorded in each ARS at the different floors, during run 21241.

In conclusion, even considering the power of background rejection at these very high rates, the bad performance of our reconstruction technique when using hits from only one line and the insufficient statistics do not allow to draw any conclusion from the single reconstructed upgoing track.
However we have demonstrated that our reconstruction technique works correctly with calibrated data (even at background rates about 5 times higher than those used in MC studies of Chapter 6) and is ready to be used for the analysis of data taken with more than one line, in the very near future.

Summary

The ANTARES Collaboration is building an underwater neutrino telescope in the Mediterranean Sea. Its aim is detecting high energy neutrinos (from 10 GeV up to the PeV region), to open a promising new window in neutrino astronomy.
One of the physics targets of the experiment is the detection of a signal from hypothetical SUSY DM annihilation in the core of celestial bodies. These expected low energy (10 GeV-10 TeV) events require a dedicated trigger and reconstruction strategy, to be deeply studied before achieving the construction of the detector and starting an observation campaign.

The improvement of the reconstruction technique, involving in detail the efficiency and the purity of the signal, has been the main concern of this thesis. Therefore the first part of the work has been devoted to a full analysis of the data taken with the MILOM prototype detector, to understand the properties of the optical background and use them in the following physics MC simulations. The results obtained were summarized in an Internal Note, presented at a Collaboration meeting and included in a paper reporting MILOM data analysis, to be submitted to publication in spring 2006.

The second part of the work focused on the study of the Prefit 1D reconstruction technique, which has been optimized to detect neutrinos from interesting candidate point sources and to separate this signal from atmospheric neutrinos and muons. Also these results were presented at a Collaboration meeting. They obtained their best acknowledgement when the reconstruction technique proved to work correctly on data taken with the first operational line of the ANTARES detector.

Our improved strategy is ready to be used for the analysis of full detector data and to hopefully give hints for a deeper understanding of our Universe.

Acknowledgements

This thesis is the result of the hard work I made in the last 10 months as a student at Università di Pisa. However my first contact with the ANTARES experiment is dated back to two years ago, when I spent one month at NIKHEF, Amsterdam as summer student.
In Amsterdam I also fixed the guidelines of my work, during a longer visit made in the context of my thesis project. Thus I would like to thank all the members of the NIKHEF ANTARES group, in particular: Claudine Colnard, who first kindly introduced me to the experiment; Els de Wolf, who took care of me at NIKHEF and worked to make my visits possible; Gordon Lim, who I shared the best part of my physics analysis with; Ronald Bruijn, for all the times he helped me in solving problems; Guus Wijnker, my favourite office mate; Bram van Rens, for all the weekends spent together at NIKHEF; Gerard van der Steenhoven, for his precious suggestions and support; and Maarten de Jong, for his exceptional insight into the physics of our experiment and for everything I could learn from him.
After the "training" period that I spent in Amsterdam, my main analysis work was done at INFN in Pisa, with the collaboration of Ersilio Castorina, Elisa Falchini and Luca Maccione.
My last, but of course not least, acknowledgement is for my supervisor Vincenzo Flaminio, who trusted my work, gave important advice and encouraged all my efforts.

Pisa, 29/03/2006

Bibliography

[1] J. L. Tonry *et al.*, *Astrophys. J.*, 594:1-24, 2003.

[2] D. N. Spergel *et al.*, *Astrophys. J. Supp.* **148**, 175 (2003).

[3] O. Laha, R. Liddle in S. Eidelman *et al.*, *Phys. Lett.* **B52**, 1 (2004).

[4] A. H. Broeils, K. G. Begeman and R. H. Sanders, *Mon. Not. R. Astr. Soc.*, 259:523, 1991.

[5] S. Burles and D. Tytler, *Astrophys. J.*, 507:732-744, 1998.

[6] R. Bernabei *et al.*, *Riv. Nuovo Cim.* **26**:1-73, 2003.

[7] D. S. Akerib *et al.*, *Phys. Rev.* **D68**:082002, 2003.

[8] P. Fayet and S. Ferrara, *Phys. Rep.* **32** (1977) 249; M. F. Sohnius, *Phys. Rep.* **128** (1985) 41; H. P. Nilles, *Phys. Rep.* **110** (1984) 1; H. E. Haber and G. L. Kane, *Phys. Rep.* **117** (1985) 75; A. B. Lahanas and D. V. Nanopoulos, *Phys. Rep.* **145** (1987) 1.

[9] J. Wess and J. Bagger, *Supersymmetry and Supergravity*, Princeton Univ. Press, 1983.

[10] P. West, *Introduction to Supersymmetry and Supergravity*, World Scientific, 1986.

[11] S. J. Gates, M. Grisaru, M. Rocek and W. Siegel, *Superspace or One Thousand and One Lessons in Supersymmetry*, Benjamin & Cummings, 1983.

[12] S. Weinberg, *The quantum theory of fields. Vol. 3: Supersymmetry*, Cambridge, UK: Univ. Press, 2000.

[13] S. Bethke, *J. Phys.* **G26** (2000) R27; hep-ex/0004021.

[14] U. Amaldi, W. de Boer and H. Furstenau, *Phys. Lett.* **B260** (1991) 447.

[15] Juergen Brunner: *Simulation of ^{40}K signals*, ANTARES-Site/1999-002.

[16] A. S. Cussatlegras: *Dynamique spatio temporelle de la bioluminesccence marine en Mer d Alboran et sur le Plateau Continental Atlantique Francais*, PHD-thesis, 2001.

[17] Vincent Bertin: *Technical description of the MILOM*, ANTARES Technical notes, 3 INS 05 03 A.

[18] Maarten de Jong: *The ANTARES Trigger Software*, ANTARES-Soft/2005-005.

[19] K. Kuzmin, T. Montaruli, I. Sokalski: *GENHEN v6r3: implementation of the Glashow resonance and of MUSIC transport code*, ANTARES-Soft/2004-012.

[20] D. Bailey: *KM3 v2r1: User Guide*, ANTARES-Soft/2002-006.

[21] J. Brunner: *GeaSim: User Manual*, http://antares.in2p3.fr/internal/software/geasim.html.

[22] Aart Heijboer: *Track reconstruction and point source searches with ANTARES*, PhD Thesis.

[23] D. Bailey: *Genhen v5r1: software documentation*, ANTARES-Soft/2002-004.

[24] Maarten de Jong: *The Summary Timeslice Writer program*, ANTARES-Soft/2005-005.

[25] Jurgen Brunner: *Updated tag list fot the new ANTARES event format*, ANTARES-Soft/1999-003.

[26] Alexander Kappes, Uli Katz: *On the use of Event Weights for the simulation of atmospheric muons in ANTARES*, ANTARES-Soft/2005-003.

[27] E. Korolkova, L. Thompson: *MonteCarlo Simulation of Cosmic Ray Muons at Sea Level with CORSIKA*, ANTARES-Soft/2003-002.

[28] R. Bruijn: *Muon reconstruction with ANTARES LINE1 data*, Internal Note to be published.